Multiple Topological States in Iron-Based Superconductors

Peng Zhang[a], Yukiaki Ishida[a], Kazuki Sumida[b], Shilong Wu[b], Koji Miyamoto[b], Taichi Okuda[b] and Shik Shin[a]

[a]*Institute for Solid State Physics, University of Tokyo, Kashiwa, Japan.*
[b]*Hiroshima Synchrotron Radiation Center, Hiroshima University, Higashi-Hiroshima, Japan*

Keywords: topological states, iron-based superconductor.

Topological materials and unconventional iron-based superconductors are both important areas of study but, to date, relatively little overlap has been identified between these two fields. However, the combination of topological bands and superconductivity promises the manifestation of exotic superconducting states, including Majorana fermions, the central component of topological quantum computation. Here, using high-resolution spin-resolved ARPES, we have identified topological insulator (TI) and Dirac semimetal (TDS) states near the Fermi energy in different iron-based superconducting compounds, potentially allowing access to several different superconducting topological states in the same material. These results reveal the generic coexistence of superconductivity and multiple topological states in iron-based superconductors, indicating that this broad class of materials is a promising platform for high-temperature topological superconductivity.

The topological Dirac semimetal states in Fe(Te,Se).

In the previous papers, we resolved the TI surface states and its related topological superconductivity at the surface of Fe(Te,Se) [1,2]. Actually, according to the calculations, TI and TDS states should appear in a pair: the TI states below E_F and the TDS states above E_F, as shown in Fig. 1a. Since it is difficult to dope Fe(Te,Se)
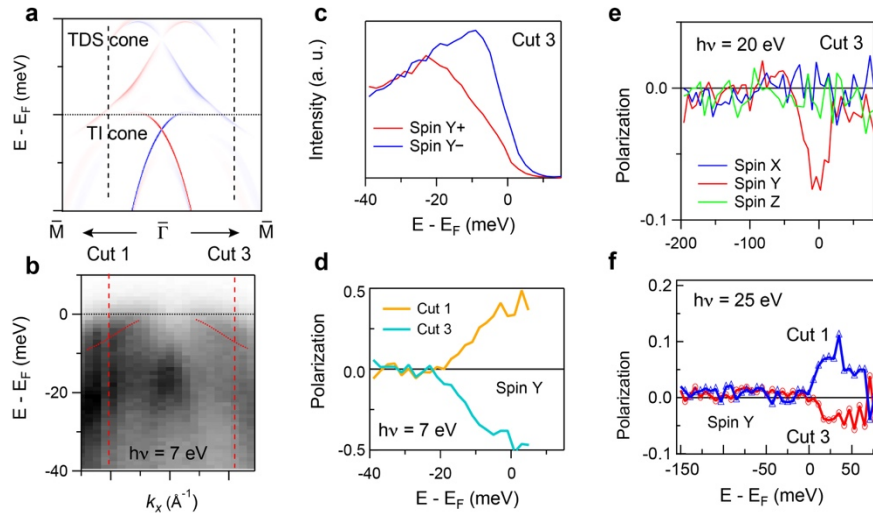
FIGURE 1. a. Theoretical calculations show that there are two Dirac cones in Fe(Te,Se): One is the surface band of TI; the other is from the surface component of TDS. **b**. ARPES intensity plot of the band structure with a 7eV laser. According to panel a, the band at E_F should be partly spin polarized. **c**. Spin-resolved EDCs at Cut 3 with a 7eV laser **d**. Spin polarization along *y* direction at Cuts 1 and 3. **e**. Spin polarization along different directions at Cut 3 measured in HiSOR with 20 eV photons. **f**. Spin polarization along *y* direction at Cuts 1 and 3 measured in HiSOR with 25 eV photons.

with electrons, the TDS cone cannot be resolved by ARPES directly. However, from Fig. 1a we found that the surface component of the TDS states extends to below E_F and induces spin polarization of the band at E_F, which means that we may obtain indirect evidences of the existence of the TDS bands by measuring spin polarization. The spin-integrate ARPES intensity plot of the band structure is shown in Fig. 2b. Using spin-resolved ARPES, we checked spin polarization of two cuts in Fig. 2b with different photon energies. In Fig. 2c and 2d, we displayed the spin resolved EDCs and the spin polarization curves along y direction measured with a 7eV laser. Due to the high energy resolution of the laser ARPES, the spin polarization is very clear. The magnitude of spin polarization is about 50%, indicating coexistence of unpolarized bulk and polarized surface states.

It is well known that the photoemission process may induce extrinsic spin polarization. However, the extrinsic spin polarization generally depends on the photon polarization, photon energy or sample orientation, while intrinsic spin polarization of the electronic initial states should show the same result for different experimental setups. To confirm that the spin polarization from 7eV photons has an intrinsic origin, we further measured the spin polarization with different photon energies at BL9B endstation in HiSOR. With 20eV photons, we observed spin polarization along y direction only, consistent with calculations and data in Fig. 2d. With 25eV photons, the result is the same as the one with 7eV photons. These results from different photon energies confirm that the spin polarization indeed comes from the electronic initial states, and thus supporting the conclusion that there are TDS states above EF in Fe(Te,Se).

The topological insulator and Dirac semimetal states in Li(Fe,Co)As.

We also studied a series of Li(Fe,Co)As samples with different Co content by using laser ARPES. Form the $x = 9\%$ and 12% electron-doped samples, we directly observed both TI and TDS Dirac cones [3]. The two Dirac cones are consistent with the DFT calculations: the upper cone comes from the the surface component of the TDS state, while the lower cone comes from the TI surface states. Their surface nature is also confirmed by the spin-resolved experiments with a 7eV laser. These results provide further support to the existence of TDS states in Fe(Te,Se).

Our findings of the TI and TDS states in Fe(Te,Se) and Li(Fe,Co)As prove the generic existence of different types of topological states in iron-based superconductors. Their simple structures, multiple topological states, and a tunable Fermi level make iron-based superconductors ideal platforms for the study of topological superconductivity, Majorana bound states, and as such, potentially, topological quantum computation.

REFERENCES

1. Z. Wang et al., *Phys. Rev. B* 92, 115119 (2015).
2. P. Zhang et al., *Science* 360, 182 (2018).
3. P. Zhang et al., *Nature Phys*. 15, 41 (2019).

Experimental observation of node-line-like surface states in LaBi

B. Feng[a], J. Cao[b], M. Yang[c], Y. Feng[a,d], S. Wu, B. Fu[b], M. Arita[a], K. Miyamoto[a], S. He[d], K. Shimada[a], Y. Shi[c], T. Okuda[a], and Y. Yao[b]

[a]Hiroshima Synchrotron Radiation Center, Hiroshima University, 2-313 Kagamiyama, Higashi-Hiroshima 739-0046, Japan
[b]Beijing Key Laboratory of Nanophotonics and Ultrafine Optoelectronic Systems, School of Physics, Beijing Institute of Technology, Beijing 100081, China
[c]Institute of Physics, Chinese Academy of Sciences, Beijing 100190, China
[d]Ningbo Institute of Materials Technology and Engineering, Chinese Academy of Sciences, Ningbo 315201, China
[e]Graduate School of Science, Hiroshima University, 1-3-1 Kagamiyama, Higashi-Hiroshima 739-8526, Japan

Topological semimetals represent a novel class of quantum materials whose conduction and valence bands touch at discrete points or extended lines [1-4]. Until now, three types of topological semimetals have been discovered: Dirac, Weyl, and nodal line. In Dirac/Weyl semimetals, the energy-momentum dispersion is linear along all momentum directions, forming Dirac/Weyl cones in the proximity of the Fermi level. In nodal line semimetals, the crossing points form extended lines in the momentum space, i.e., the nodal lines. While the Dirac cones or nodal lines discovered in topological semimetals typically derive from the bulk bands, an interesting question is whether they can exist as surface states of three-dimensional crystals. The nodal line surface states could manifest extraordinary properties that are distinct from other two-dimensional Dirac materials [5-7]. To date, the surface Dirac cones have already been extensively studied in topological insulators, such as the Bi_2Se_3 family materials, while theoretical and experimental studies on the surface nodal lines are still rare.

Recently, rare-earth monopnictide LaBi has been predicted to be a topological insulator based on first-principles calculations. Moreover, magnetotransport measurements showed that LaBi hosts extremely large magnetoresistence (XMR), in analogy to some topological semimetals, such as Cd_3As_2, TaAs, and ZrSiS. These results have stimulated great research interest to search for the Dirac bands in LaBi. Recent angle-resolved photoemission spectroscopy (ARPES) measurements revealed that there are multiple surface Dirac cones on the (001) surface of LaBi. However, the details of the band structures are still controversial. Nayak *et al.* and Niu *et al.* reported two surface Dirac cones at the $\bar{X}$ point with an energy separation of 75 and 190 meV, respectively. In contrast, Lou *et al.* reported only one Dirac cone at the $\bar{X}$ point. Therefore, clarifying these controversies, which is essential to understand the extraordinary transport properties in LaBi, calls for further experimental and theoretical efforts.

Here, we present the results of high-resolution ARPES measurements and first-principles calculations on the electronic structures of LaBi. We find that the surface states near the $\bar{X}$ points resemble Dirac nodal lines. Our calculations show that these node-line-like bands are slightly gapped because of the hybridization of surface states, but the gap is beyond our experimental resolution. These results may provide important information to understand the extraordinary physical properties in LaBi and could stimulate further research interest to search for the exotic physical properties associated with nodal line fermions.

The photoemission intensity of the Fermi surface of LaBi is shown in Fig. 1(c), which includes several Fermi pockets at the $\bar{\Gamma}$ and $\bar{X}$ points of the surface BZ. Figure 1(d) shows the measured band structures along the $\bar{\Gamma}$-$\bar{X}$ direction. At the $\bar{\Gamma}$ point, we observe a Dirac-like band with the crossing point located at approximately 0.1 eV below the Fermi level, as indicated by the red arrow.

We then focus on the band structures near the $\bar{X}$ point. Figure 2 shows the band structures along a series of parallel cuts in the proximity of the $\bar{X}$ point, as indicated by the red lines in Fig. 1(c). One can see that there is a linear band crossing along each cut without any detectable gap feature. The Fermi velocity is approximately 7×10^5 m·s^{-1}, which is comparable to that in graphene. From cut 1 to cut 12, the crossing point gradually moves from E_B=0.23 eV (cut 1) to E_B=0.14 eV (cut 7), and then moves back to higher binding energies. These results indicate that there is a Dirac nodal line that goes through the $\bar{X}$ point. The nodal line is along the $\bar{\Gamma}$-$\bar{X}$ direction and has a weak dispersion. According to the C_4 rotational symmetry of the $\bar{X}$ point, there must be a perpendicular nodal line crossing the $\bar{X}$ point, but its intensity is much weaker because of the matrix element effect.

This work has been published in Physical Review B **97**, 155153 (2018).
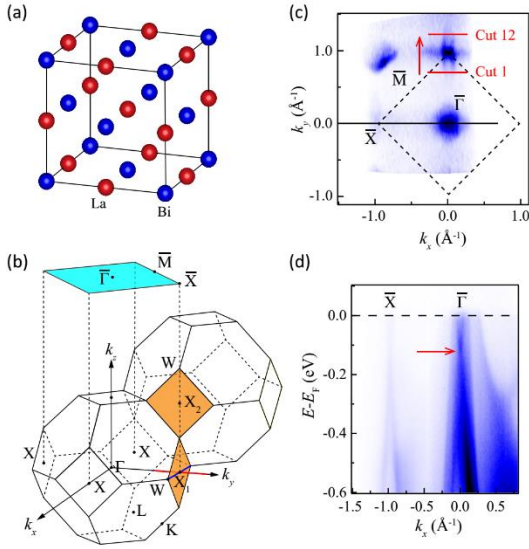
FIGURE 1. Crystal structure of LaBi. Red and blue balls represent La and Bi atoms, respectively. (b) Bulk Brillouin zone and the (001)-projected surface Brillouin zone. The calculated band structures along the blue and red lines are shown in Figs. 4(a) and 4(b), respectively. (c) Photoemission intensity at the Fermi level of LaBi measured with 31-eV photons. Red lines indicate the momentum cuts along which the ARPES intensity plots in Fig. 2 were taken. (d) ARPES intensity plot along the black line in (c). From Ref. 8.

FIGURE 2: ARPES intensity plots near the $\bar{X}$ points. The data were taken along the red lines in Fig. 1(c). Cut 7 corresponds to the one that goes through the $\bar{X}$ point. From Ref. 8.
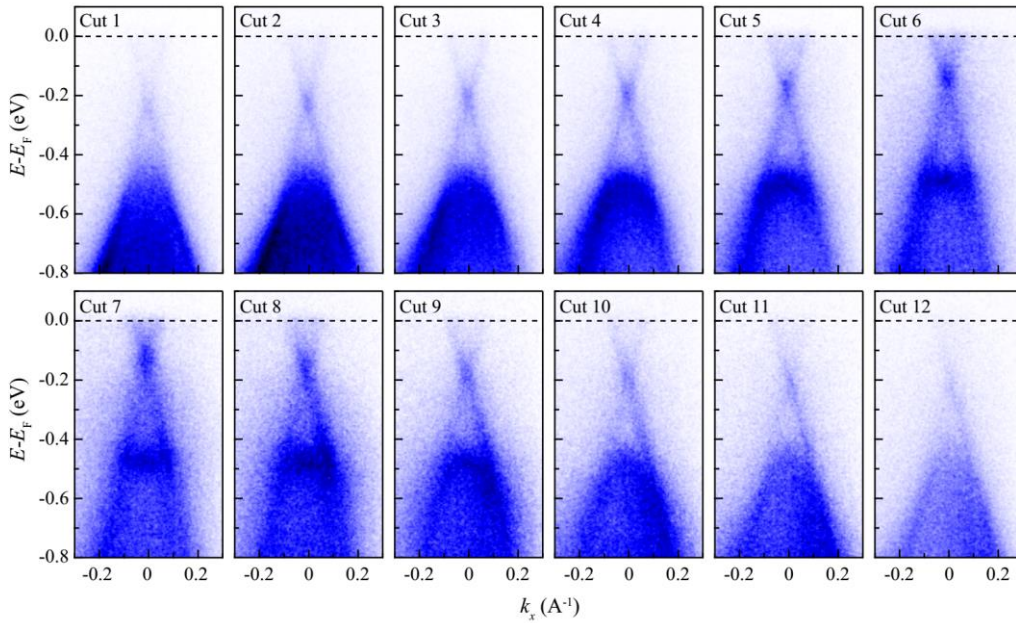
REFERENCES

1. S. M. Young, S. Zaheer, J. C. Y. Teo, C. L. Kane, E. J. Mele, and A. M. Rappe, Phys. Rev. Lett. 108, 140405 (2012).
2. Z. Wang, Y. Sun, X.-Q. Chen, C. Franchini, G. Xu, H. Weng, X. Dai, and Z. Fang, Phys. Rev. B 85, 195320 (2012).
3. Z. K. Liu, B. Zhou, Y. Zhang, Z. J. Wang, H. M. Weng, D. Prabhakaran, S.-K. Mo, Z. X. Shen, Z. Fang, X. Dai, Z. Hussain, and Y. L. Chen, Science 343, 864 (2014).
4. S. Xu, I. Belopolski, N. Alidoust, M. Neupane, G. Bian, C. Zhang, R. Sankar, G. Chang, Z. Yuan, C.-C. Lee, S.-M. Huang, H. Zheng, J. Ma, D. S. Sanchez, B. Wang, A. Bansil, F. Chou, P. P. Shibayev, H. Lin, S. Jia, and M. Z. Hasan, Science 349, 613 (2015).
5. B. Feng, B. Fu, S. Kasamatsu, S. Ito, P. Cheng, C.-C. Liu, Y. Feng, S. Wu, S. K. Mahatha, P. Sheverdyaeva, P. Moras, M. Arita, O. Sugino, T.-C. Chiang, K. Shimada, K. Miyamoto, T. Okuda, K. Wu, L. Chen, Y. Yao, and I. Matsuda, Nat. Commun. **8**, 1007 (2017).
6. A. K. Geim and K. S. Novoselov, Nat. Mater. **6**, 183 (2007).
7. A. H. Castro Neto, F. Guinea, N. M. R. Peres, K. S. Novoselov, and A. K. Geim, Rev. Mod. Phys. **81**, 109 (2009).
8. B. Feng, J. Cao, M. Yang, Y. Feng, S. Wu, B. Fu, M. Arita, K. Miyamoto, S. He, K. Shimada, Y. Shia, T. Okuda, and Y. Yao, Phys. Rev. B **97**, 155153 (2018).

Observation of Bulk and Surface Spin-Orbital Textures in Nonsymmorphic NbGeSb

Igor Marković[1], O. Clark[1], S. Wu[2], T. Okuda[3], K. Murphy[4], J. Alaria[4], P. King[1]

[1]*SUPA, School of Physics and Astronomy, University of St Andrews, St Andrews, KY16 9SS, UK*
[2]*Graduate School of Science, Hiroshima University, Higashi-Hiroshima, Japan*
[3]*Hiroshima Synchrotron Radiation Center, Hiroshima University, Higashi-Hiroshima, Japan*
[4]*Department of Physics, University of Liverpool, Liverpool L69 7ZE, UK*

Keywords: Rashba, nonsymmorphic, NbGeSb, SARPES.

In recent years the interplay of spin-orbit coupling (SOC) and crystalline symmetries has been extensively explored as a driving mechanism for developing novel electronic band structures in solids. The realisation by Young and Kane [1] that nonsymmorphic symmetries can stabilise the intersection point of topologically trivial and non-trivial states of matter has opened new paradigms for creating and manipulating bulk Dirac systems. Yet experimentally, the role of spin-orbit coupling in those systems has remained elusive. Here, we investigate this interplay in NbGeSb, a member of the nonsymmorphic ZrSiS family of Dirac nodal line semimetals [2-5]. In particular, we use spin- and angle-resolved photoemission spectroscopy (SARPES) to disentangle the complex bulk and surface electronic structure of this compound. Building on our previous observation of two sets of surface electronic states in this compound, we sought to uncover their detailed and strongly intertwined spin-orbital textures.

These surface states disperse within a large bulk-projected band gap along the Brillouin zone edge, while they become resonant with the bulk states with approaching the Brillouin zone centre (Fig. 1). Similar surface states have been observed in the structurally equivalent (Zr,Hf)SiS systems [2,4,5], and a detailed investigation [2] showed that they emerge from the bulk manifold due to the breaking of the nonsymmorphic symmetry at the cleavage plane of the material. Due to different distribution of valence electrons, we observe how the surface states move much further away from their parent bulk manifolds in NbGeSb, leading to them intersecting in the vicinity of E_F (Fig. 1b). Using spin-resolved measurements performed at BL-9B, we showed that these surface states are spin-polarised, exhibiting spin splittings of the Rashba type. The magnitude of the spin splitting is comparable to the size of atomic SOC energy scales for the relevant orbitals. Moreover, through systematic measurements of the vectorial spin texture, we have uncovered how the high symmetry of the surface unit cell leads to a highly structured spin texture of the surface state Fermi surface (Fig.1a). These findings are of key importance for understanding the influence of spin-orbit coupling in this system, and the determination of the spin-orbital textures of these states, and their role in shaping the band degenerices which this system hosts.
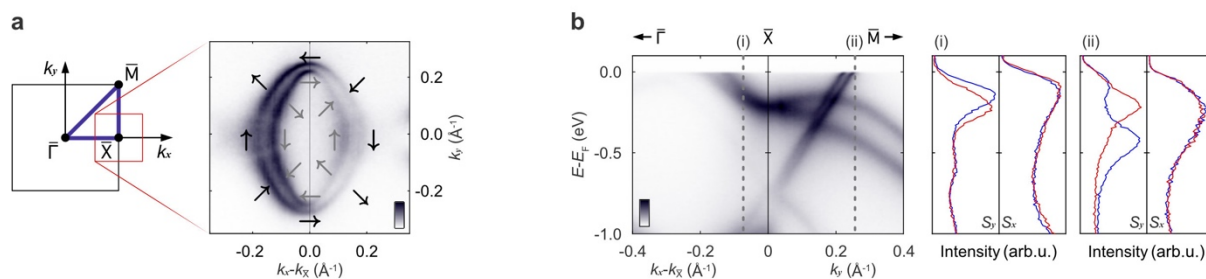
FIGURE 1. (a) Brillouin zone and surface state Fermi surface, with spin textures shown schematically. (b) Band dispersions in the vicinity of X, with spin-resolved EDCs (right) measured along the dotted lines shown.

REFERENCES

1. S. M. Young *et al.*, *Phys. Rev. Lett.* **115** (2015) 126803
2. A. Topp *et al.*, *Phys. Rev. X* **7**, (2017) 041073
3. C. Chen *et al.*, *Phys. Rev. B* **95**, (2017) 125126
4. L. Schoop *et al.*, *Nature Commun.* **7**, (2016) 11696
5. D. Takane *et al.*, *Phys. Rev. B* **94**, (2016) 121108

Spin-resolved photoemission studies on possible half-metallic SrRuO3 thin film

Hanyoung Ryu[a,b] , Saikat Das[a,b], Bongju Kim[a,b], Changyoung Kim[a,b], and Taichi Okuda[c]

[a]Center for Correlated Electron Systems, Institute for Basic Science, Seoul 08826, Korea
[b]Department of Physics and Astronomy, Seoul National University, Seoul, 08826, Korea
[c]Hiroshima Synchrotron Radiation Center (HSRC), Hiroshima University, Higashi-Hiroshima 739-0046, Japan

Half-metals with fully spin-polarized conduction electrons are a promising candidate for spintronic applications. While the ferromagnetic metals are abundant, the half-metallic ferromagnets are limited in numbers, with examples include CrO_2, $La_{0.7}Sr_{0.3}MnO_3$, NiMnSb, and Co_2FeSi [1]. It is, therefore, of practical interest to explore new materials that are believed to be close to half-metallic (HM) ground states.

$SrRuO_3$ (SRO) is an itinerant ferromagnet (with $T_c \sim 165$ K), and in bulk is considered to just miss the half-metallic ground state due to the lack of strong exchange-correlation [1,2]. Several proposals are put forward to artificially drive the system to the HM state either by spatially confining the carriers or by heterostructuring in the honeycomb motif [3-5]. A recent attempt following the former route yielded a ferromagnetic metallic state with decreased T_c while no information is available on the resulting spin-polarization [6]. On the contrary, the latter approach remains unexplored.
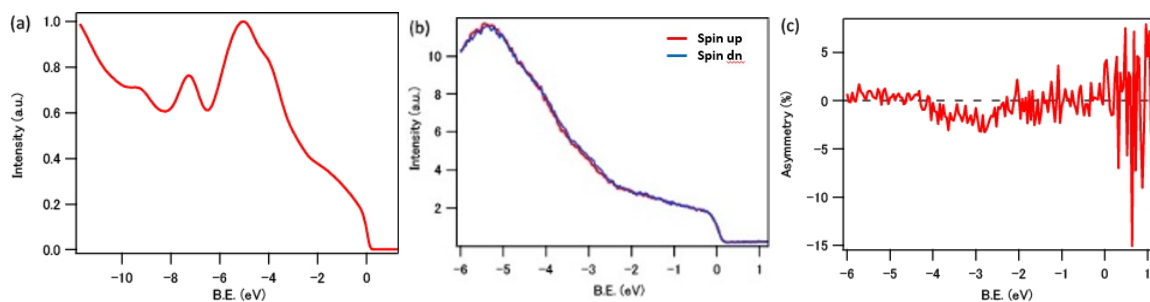
FIGURE 1. (a) The angle integrated spectra of SrRuO3(111) film taken with 21 eV linearly polarized photon. (b) Spin-resolved spectra taken with 21 eV photon at Γ point of the Brillouin zone. The red (blue) curve is intensity from plus (minus) spin. (c) The asymmetry, extracted from the figure (b) exhibiting vanishingly small spin-asymmetry.

Motivated by these considerations, we explored SRO thin films (~ 30 nm thick) grown on the (111)-oriented $SrTiO_3$ substrates, which form the basis of the honeycomb motif. Thin films were grown using the pulsed laser deposition (PLD) technique and subsequently capped with Se to prevent direct exposure to the ambient. To remove the Se-capping layer, the films were annealed in the preparation chamber at a temperature of about 450° C at a base pressure of 10^{-8} Torr. Subsequently, the films were transferred to the ARPES chamber, where we performed spin-resolved photoemission spectroscopy (spin-PES) measurements at a temperature of 20K with a photon energy of 21 eV. To completely magnetize the films, we cooled down the films in a magnetic field applied parallel to the surface normal (along the easy axis of the films).

Figure 1 (a) shows the angle-integrated photoemission spectrum taken up to binding energy of 12 eV below the Fermi energy. Meanwhile, Fig. 1(b) displays the corresponding spin-resolved spectra that are

obtained for two opposite polarities of the spin-detector. In Fig. 1(c) we plot the spin-asymmetry extracted from Fig. 1 (b). Despite being a robust ferromagnet, the spin-PES exhibits no discernable spin-asymmetry around the Fermi energy level. Such absence of spin-asymmetry might stem from two factors. First, the presence of a contamination layer in the form of the thin Se capping layer, that reduces the spin polarization of photo-excited electrons. Second, for the given photon energy (~21 eV), we probed bands with negligible spin-splitting. More careful studies, with cleaner surface are thus required to elucidate the nature of ferromagnetic ground state of (111)-oriented SRO films, and extract the exact spin-polarization value.

REFERENCES

1. M. I. Katsnelson et al., Rev. Mod. Phys. 80, 315 (2008).
2. I. I. Mazin and D. J. Singh, Phys. Rev. B 56, 2556 (1997).
3. Marcos Verissimo-Alves et al., Phys. Rev. Lett. 108, 107003 (2012).
4. James M. Rondinelli et al., Phys. Rev. B 78, 155107 (2008).
5. L. Si et al., Phys. Rev. Lett. 119, 026402 (2017).
6. H. Boschker et al., Physical Review X 9, 011027 (2019).

Spin resolved Dirac cone surface state in trigonal layered PtBi$_2$

YaFeng[a], Shaozhu Xiao[a], Kenya Shimada[b], Shaolong He[a]

aNingbo Institute of Materials Technology and Engineering,
Chinese Academy of Sciences, Ningbo 315201, China

bHiroshima Synchrotron Radiation Center, Hiroshima University, Higashi-Hiroshima 739-0046, Japan

Keywords:trigonal PtBi$_2$, surfacestate , Diraccone, spin texture

The trigonal PtBi$_2$ has attracted great interest since it has been recently reported as a possible candidate for triply degenerate pointfermions [1]. Here we measured band structure of PtBi$_2$on BL-9B by spin resolved ARPES and found a spin polarized surface states at Γ point.
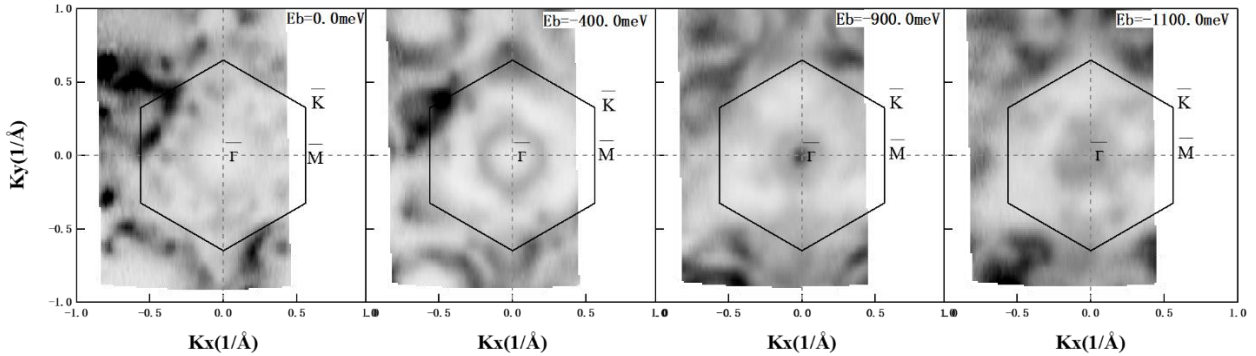
FIGURE 1. Constant energy contours of trigonal PtBi$_2$, hv=28eV.

The material we measured here is trigonal PtBi$_2$ which is different from former reported hexagonal PtBi$_2$ [2-4]. The trigonal PtBi$_2$ belongs to P31m space group while hexgonal PtBi$_2$ belongs to P-3 space goup. We determined its space group by single crystal analysis using XRD (X-ray diffraction) data which will be published elsewhere. The most important difference between them is that the hexagonal PtBi$_2$ is inversion symmetric while the trigonal one isn't. FIGURE1shows theconstant energy contours of trigonalPtBi$_2$ measured by ARPES with hv=28eV.There is an electron pocket at Γpoint which shrinks to a point at Eb≈0.9eV and then becoms to a small circle at Eb=1.1eV. This trend suggests that it should be a cone.
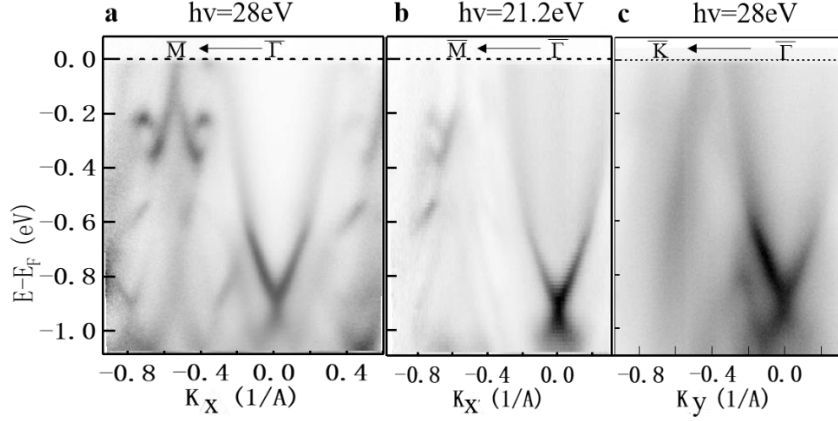
FIGURE 2. Band structures of trigonal PtBi$_2$ along high symmetric directions under different photon energies. **a**, dispersion along $\overline{\Gamma}$ –$\overline{M}$ direction , hv=28eV. **b**, dispersion along $\overline{\Gamma}$–$\overline{M}$ direction, hv=21.2eV. **c**, dispersion along $\overline{\Gamma}$ - $\overline{K}$ direction, hv=28eV.

FIGURE 2**a** and **b** show dispersions along the same direction $\overline{\Gamma}$ –$\overline{M}$. FIGURE 2**c** shows the dispersion along $\overline{\Gamma}$ -$\overline{K}$. There is a crossing point at $\overline{\Gamma}$ point with Eb≈0.9eV respectively in **a** , **b** and **c**, which, associated with FIGURE 1, indicates the presence of a Dirac cone at $\overline{\Gamma}$ point. Moreover, no variation with different photon energies implies that it's mainly from surface state.

To further confirm whether it's a Dirac cone or not, we measured its spin texture. FIGURE 3**a** shows the enlarged E-k image along $\overline{\Gamma}$ -$\overline{M}$ direction measured by ARPES. The spin polarized EDCs (energy distribution curves) along line 1(blue dashed line1 in FIGURE 3**a**) are shown in FIGURE 3**b1** and FIGURE 3**c1** along different spin directions. The spin polarized EDCs (energy distribution curves) along line 2(blue dashed line2 in FIGURE 3**a**) are shown in FIGURE 3**b2** and FIGURE 3**c2** along different spin directions. The red (blue) lines in FIGURE 3**b** and FIGURE 3**c** stand for intensity along positive (negative) direction. Finally, we can get the spin polarization (green lines) along Y axis and Z axis in FIGURE 3**b** and FIGURE 3**c** respectively. Comparing FIGURE 3**b1** and FIGURE 3**b2**, it's can be concluded that the spin polarization is opposite at Eb=0.7eV along Y axis while there is no spin polarization along Z axis. The Y axis is inside the sample surface and perpendicular to the slit of the electron energy analyzer. The Z axis is normal to the sample surface. So the spin polarization of the band is consistent with that of a Dirac cone surface state.
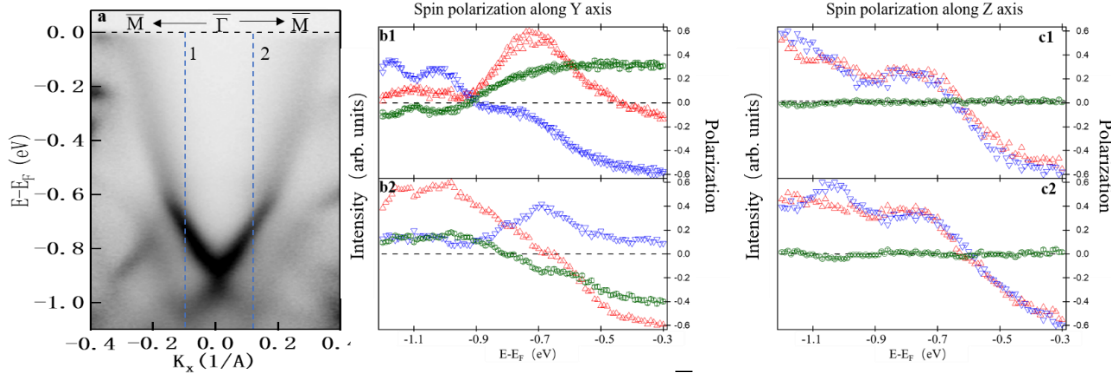
In summary, we observed a Dirac cone surface state at $\overline{\Gamma}$ point of trigonal PtBi$_2$. We found it's spin polarized along Y axis and not spin polarized along Z axis. Moreover, the spin polarization along Y axis is opposite at opposite k, which means its spin and momentum are locked.

REFERENCES

1. Wenshuai Gao et al, *Nat. Comm.* 9, 3249 (2018).
2. Yao, Q. et al. Phys. Rev. B 94, 235140 (2016).
3. Thirupathaiah, S. et al. Phys. Rev. B 97, 035133 (2018).
4. Yang, X. et al. Appl. Phys. Lett. 108, 252401(2016).

Electronic and spin structure of Bi-graphene-like system

V.A. Golyashov[a], A. Kimura[b], T. Okuda[c], O.E. Tereshchenko[a,d]

[a]*Institute of Semiconductor Physics Siberian Branch, Russian Academy of Sciences, pr.Akademika Lavrent'eva 13, Novosibirsk, 630090 Russian Federation*
[b]*Hiroshima Synchrotron Radiation Center, Hiroshima University, 2-313 Kagamiyama, Higashi-Hiroshima 739-0046, Japan*
[d]*Graduate School of Science, Hiroshima University, 1-3-1 Kagamiyama, Higashi-Hiroshima 739-8526, Japan*
[e]*Novosibirsk State University, ul.Pirogova2, Novosibirsk, 630090 Russian Federation*

Keywords: Bi, InAs, electronic structure, spin- and angle-resolved photoemission

The ultrathin film of group-V semimetal bismuth (Bi) is a promising candidate to investigate the graphene-like properties and surface Rashba effect, since the energy splitting of the bands is fairly large owing to the heavy atomic mass of the Bi atom. For the technological purposes InAs semiconductor is of special interest because it exhibits downward band bending leading to an accumulation of electrons at the surface, having characteristic of 2DEG. Such 2DEGs demonstrated many interesting and fundamental phenomena such as the integer and fractional Hall effect [1], 2D superconductivity [2] as well as technological importance in devices such as metal–oxide–semiconductor field-effect transistor and high electron mobility transistor.

The aim of this work is to develop the methods of preparation (substrate surface preparation, evaporation rate, …) and to study the electronic structure of Bi/InAs(111) interfaces using state-of-the-art spin- and angular resolved photoemission spectroscopy (SR ARPES) with synchrotron radiation at BL-9B.
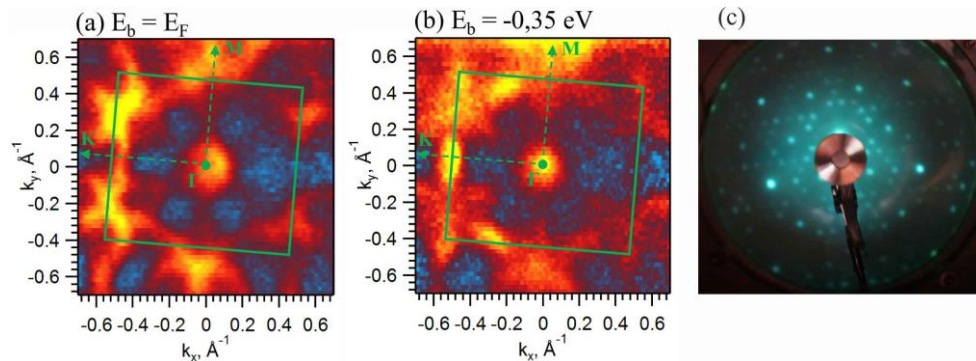
FIGURE 1 Fermi surface mapping of around Γ point (a) and E_F-E_b=0.35 eV (b) at hv=23 eV of the bismuth monolayer on InAs(111)A surface. (c) LEED pattern on Bi/InAs(111)A-(2√3x3)Bi surface.

Fig.1 shows the Fermi surface mapping of Bi/InAs(111)A-(2√3x3)Bi surface. At 1 ML of Bi coverage the InAs(111)A-(2√3x3)Bi structure is formed which consist of three 60º oriented domains. The electronic structure of InAs(111)A-(2√3x3)Bi surface is significantly different from those observed on InAs(111)A-(1x1)Bi. The dispersion contains a small gap, which can be considered in the first approximation as a gap in the primarily Rashba states.The appearance of a gap is probably induced by the strong spin-orbit interaction in bismuth layer and reduced structural surface symmetry. The observed dispersion can be interpreted as the graphene-like Dirac state with a gap. Spin-resolved measurements confirmed the spin polarization in upper and bottom branches of the cones depending on the momentum direction.

REFERENCES

1. K. von Klitzing, et al., Phys. Rev. Lett. 45, 494 (1980).
2. N. Reyren, et al., Science317, 1196 (2007).

Spin Polarized Electronic Structure of Metal Overlayers on Magneto-Electric Cr_2O_3

Takashi Komesu[a], M. Kakoki[b], T. Okuda[c], K. Miyamoto[c],
Prescott E. Evans[a] and Peter A. Dowben[a]

[a]*Department of Physics and Astronomy, Theodore Jorgensen Hall, 855 N 16th, University of Nebraska, 880299, Lincoln, NE 68588-0299, U.S.A.*
[b]*Graduate School of Science, Hiroshima University, Higashi-Hiroshima, Hiroshima 739-6526*
[c]*Hiroshima Synchrotron Radiation Center, Hiroshima University, Higashi-Hiroshima 739-0046, Japan*

Keywords: Spin Polarized Photoemission Spectroscopy, Electronic Structure.

Chromia (Cr_2O_3) continues to attract much attention as a magneto-electric material [1-8], with a Néel temperature above room temperature [1]. One interesting feature of this antiferromagnetic (AFM) is the significant boundary spin polarization at the (0001) surface [1-3,8]. This boundary polarization can be isothermally controlled to provide perpendicular voltage-controlled exchange-bias in an adjacent ferromagnet [1,4-7]. Previous investigations, on Cr_2O_3 at HiSOR beam line, successfully acquired evidence of exchange interactions for thin cobalt films with the Cr_2O_3 substrate [9]. Yet the magnetic coupling at the interface of $Co/Cr_2O_3(0001)$ leads to a more complexity magnetic interaction [6,7,9,10]. There is clear evidence from X-ray magnetic dichroism that the coupling between Co and $Cr_2O_3(0001)$ is antiferromagnetic at the interface [10]. Since the magneto-crystalline c-axis anisotropy of chromia supports a perpendicular magnetization, the interface exchange interaction can be exploited to add a perpendicular component to the Co magnetization, with antiferromagnetic coupling at the interface [9,10]. Recently, we investigated palladium (Pd) thin films on Cr_2O_3 to reveal the influence of the chromia substrate on the Pd overlayer, and the possible magnetic behavior of Pd that has been realized under some conditions [11].

For the spin polarized photoemission and spin polarized inverse photoemission studies, the Cr_2O_3 sample was magneto-electrically field cooled in applied E and B fields through the chromia Néel temperature (307 K), in order to put Cr_2O_3 in a single domain state and enhance the net surface polarization. Figure 1 shows, a) the Spin-Polarized Photoemission Spectra (SP-PES) for a thin Pd overlayer deposited on top of Cr_2O_3 at room temperature performed at HiSOR (BL-9B), using the very low energy electron diffraction (VLEED) spin detector as described elsewhere [12] and a photon energy of 150 eV, and b) for Spin Polarized Inverse Photoemission Spectroscopy (SPIPES). The blue (red) triangles in Figure 1 indicate spin up (down) components, respectively, and the green lines indicate the spin integrated spectra. Combining of Figure 1 (a) and (b) reveals substantial Pd spin projections on perpendicular (SP-PES) and parallel (SPIPES) component to the film plane.

The spin majority dominates the occupied density of states, as expected, but the presence both a perpendicular (Figure 1a) and in-plane (Figure 1b) component of spin polarization is a clear indication of a Pd adlayer with canted spin alignment. The canting is consistent with our previous measurement for Co and micromagnetic simulations and magnetic force microscopy. This work clarifies the mechanisms by which the anomalous Hall effect memory cell [13] works and illustrates the value of a combined investigation of the net spin polarization of both the valence (SP-PES) and conduction (SPIPES) band

electronic structure, and a first in the ongoing investigation Cr_2O_3 exchange coupling with various overlayers.
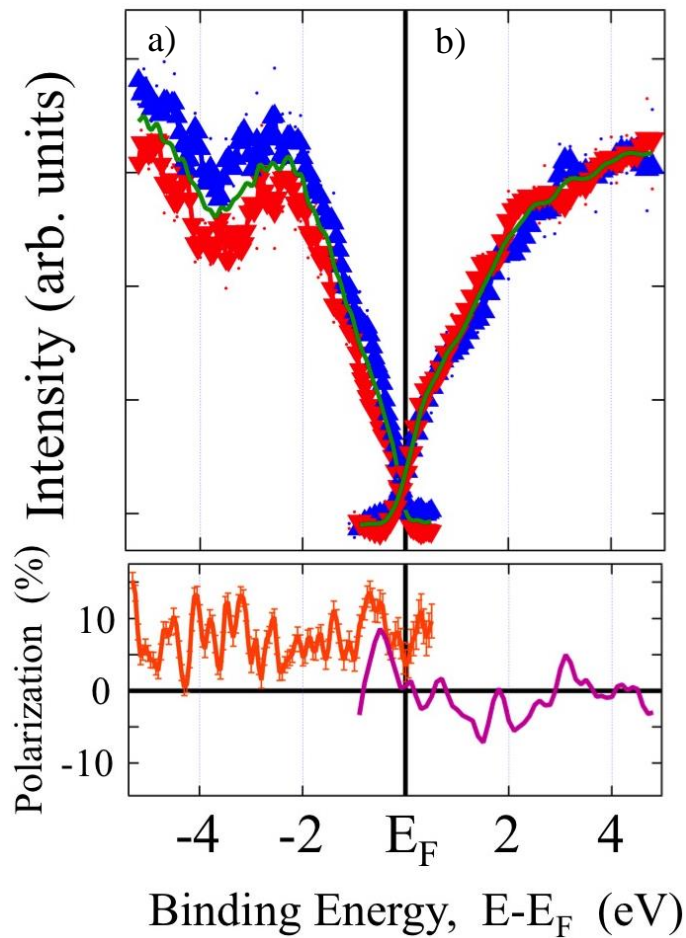
Figure 1. The spin-polarized photoemission spectra for thin Pd layer on top of Cr_2O_3: (a) the measured out of plane spin polarization for 5Å Pd and (b) spin polarized invers photoemission spectroscopy for 5Å Pd. The blue (red) triangle indicate spin up (down) components, respectively, and the green line indicates the spin-integrated spectra. Bottoms are polarization of spins.

References

[1]   X. He, Y. Wang, N. Wu, A. N. Caruso, E. Vescovo, K. D. Belashchenko, P. A. Dowben, and C. Binek, Nat. Mater. **9**, 579 (2010).

[2]   S. Cao, X. Zhang, N. Wu, A. T. N'Diaye, G. Chen, A. K. Schmid, X. Chen, W. Echtenkamp, A. Enders, Ch. Binek, P. A. Dowben, New J. Physics **16**, 073021 (2014).

[3]   N. Wu, X. He, A. L. Wysocki, U. Lanke, T. Komesu, K. D. Belashchenko, C. Binek, and P. A. Dowben, Phys. Rev. Lett. **106**, 087202 (2011).

[4]   W. Echtenkamp, and Ch. Binek, Phys. Rev. Lett. **111**, 187204 (2013).

[5]   K. Toyoki, Y. Shiratsuchi, A. Kobane, S. Harimoto, S. Onoue, H. Nomura, and R. Nakatani, J. Appl. Phys. **117**, 17D902 (2015).

[6]   T. Ashida, M. Oida, N. Shimomura, T. Nozaki, T. Shibata, and M. Sahashi, Appl. Phys. Lett. **106**, 132407 (2015).

[7]   K. Toyoki, Y. Shiratsuchi, A. Kobane, C. Mitsumata, Y. Kotani, T. Nakamura, and R. Nakatani, Appl. Phys. Lett. **106**, 162404 (2015).

[8]   K. D. Belashchenko, Phys. Rev. Lett. **105**, 147204 (2010).

[9]   R. Choudhary, T. Komesu, P. Kumar, P. Manchanda, K. Taguchi, T. Okuda, K. Miyamoto, P. A. Dowben, R. Skomski, and A. Kashyap, Europhysics Letters **115**, 17003 (2016).

[10]   Y. Shiratsuchi, Y. Kotani, S. Yoshida, Y. Yoshikawa, K. Toyoki, A. Kobane, R. Nakatani, and T. Nakamura, AIMS Materials Science **2**, 484-496 (2015).

[11]   S. Sakuragi, T. Sakai, S. Urata, S. Aihara, A. Shinto, H. Kageshima, M. Sawada, H. Namatame, M. Taniguchi, and T. Sato, Phys. Rev. B **90**, 054411 (2014).

[12]   T. Okuda, K. Miyamoto, H. Miyahara, K. Kuroda, A. Kimura, H. Namatame, and M. Taniguchi, Rev. Sci. Instrum. **82**, 103302 (2011).

[13]   T. Kosub, M. Kopte, R. Hühne, P. Appel, B. Shields, P. Maletinsky, R. Hübner, M.O. Liedke, J. Fassbender, O.G. Schmidt, D. Makarov, Nature Commun. **8**, 13985 (2017).

Insight Into The Spin-Texture Of Shockley and Dirac States Handling by Competitive Spin-Orbit and Exchange Magnetic Interactions in GdRh$_2$Si$_2$, HoRh$_2$Si$_2$, GdIr$_2$Si$_2$ and YbIr$_2$Si$_2$ materials.

Denis Vyalikh[a, b], Dima Usachov[c], Georg Poelhen[d], Andres Santander-Syro[e], Takehito Imai*, Koji Miyamoto[#], and Taichi Okuda[#]

[a]*DIPC, Paseo Manuel Lardizabal 4, Donostia San Sebastian 20018, Basque Country, Spain*
[b]*IKERBASQUE, Basque Foundation for Science, 48013 Bilbao, Basque Country, Spain*
[c]*Saint Petersburg State University, Saint Petersburg 198504, Russia*
[d]*Institut für Festkörper- und Materialphysik, Technische Universität Dresden, D-01062 Dresden, Germany*
[e] *CSNSM, Université Paris-Sud and CNRS/IN2P3, Batiments 104 et 108, 91405 Orsay, France*
Graduate School of Science, Hiroshima University, 1-3-1 Kagamiyama, Higashi-Hiroshima 739-8526, Japan
[#]*Hiroshima Synchrotron Radiation Center, Hiroshima University, 2-313 Kagamiyama, Higashi-Hiroshima 739-0046, Japan*

Our research is focused on the disentangling the properties of 2D electrons in presence of spin-orbit coupling (SOC) in combination with a lack of inversion symmetry and exchange magnetic interaction (EMI) as well as Kondo interaction. We have performed SR-ARPES measurements of 2D states for antiferromagnet (AFM) GdRh$_2$Si$_2$ (T$_N$=107 K), AFM-TbRh$_2$Si$_2$ (T$_N$=92 K), and mixed-valent EuIr$_2$Si$_2$ [1-3]. It is known that for GdRh$_2$Si$_2$, in the AFM phase the 4f moments lie inclusively *in plane,* while for TbRh$_2$Si$_2$ they are oriented along [001] direction, i.e. have *out of plane* order due to the crystal-electric-field effect. The signature for the *out of plane* order is seen in ARPES (fig. 1) as a spin-splitting of the surface states at the M-point (fig. 1b). This property has been discussed for HoRh$_2$Si$_2$ (T$_N$=29.5 K) [1], which exhibits out of plane magnetic order. We turn to Tb-system, since i) it reveals the similar properties but, ii) it has larger T$_N$, which gives a certain freedom for the experiments. The beauty of EuIr$_2$Si$_2$ [3] is that below the Si-Ir-Si surface block, the Eu ions reveal valence 2+, i. e. they have a large and pure spin moment J = S = 7/2. Below 48 K, the Eu 4fs order ferromagnetically that, together with strong SOC, essentially modifies the properties of 2D states [3]. Our aim was to explore the spin-texture of the surface states when (i) the orientation of 4f moments is changed from "in plane" (GdRh$_2$Si$_2$) to out of plane (TbRh$_2$Si$_2$), (ii) the SOC remains on the same level or (iii) is enhanced due to substitution of Rh by Ir. Combination of SOC with the EMI of 2D electrons with the ordered 4f moments of RE layer underneath the topmost Si-T-Si block opens perspectives to explore how these electrons are affected and how their properties can be controlled by means of SOC and EMI. We have obtained the experimental results for all mentioned systems and we are presently working on their evaluation, DFT calculations, and **kp** modeling [3, 4]. Here, we present the first curios observation made for Tb system. In figure 1c, we show how the spin-texture of the surface state at the M-point is seen from DFT calculations. While the out-of-plane magnetization in the Tb system was thought to be large enough in order to destroy the original in-plane spin-momentum coupling caused by the SOC, we nevertheless anticipate to experimentally disclose this in-plane coupling almost unaffected. In the fig. 2 we show the schematic view of the spin-split surface state as well as the points in *k*-space, where the SR-ARPES data were taken. The data reflecting the projection of the spin on X, Y and Z planes are shown together with the DFT modelling of the spectra. Already a first inspection of the experimental data suggests that the expected strong Z-signal is almost absent. On first sight, this result looks unclear, however, one should keep in mind that we measure the magnetically ordered system, which should possesses the magnetic-domains structure.
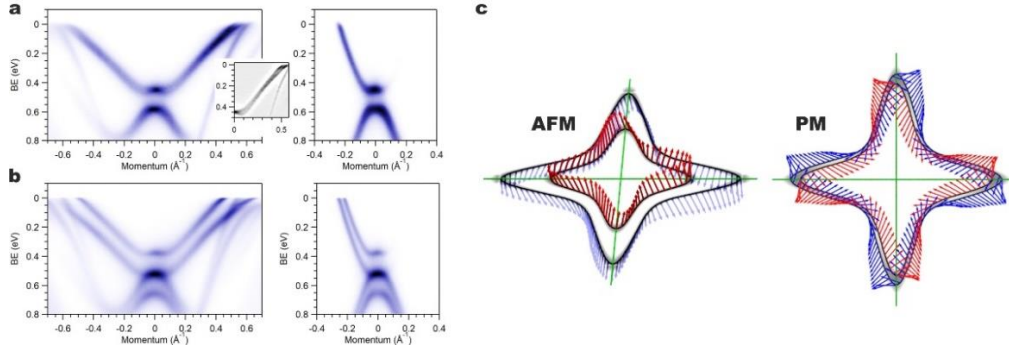
FIGURE 1. ARPES data taken from TbRh$_2$Si$_2$ in PM (a) and AFM (b) phases indicating the properties of the surface states at the M-point. The spin-splitting driven by SOC effect is clearly seen from the inset data for PM phase. The spin-texture of this surface state derived from *ab-initio* DFT calculations for both phases is shown in (c).
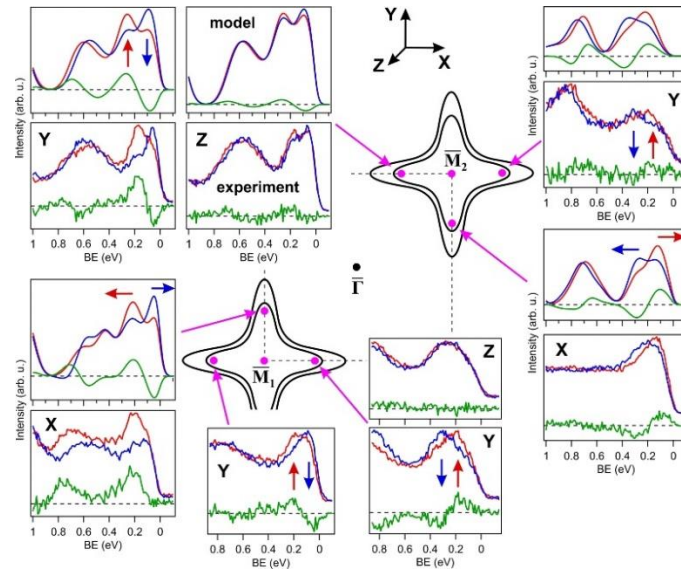
FIGURE 2. Spin-resolved ARPES data taken from TbRh$_2$Si$_2$ for AFM phase at 18 K for a few *k*-points of the surface state derived for X, Y and Z channels that reflects the projection of the spin on the respective axis.

Since the Tb system has the *out of plane* AFM order, one can reasonably assume that near the Si-surface within the topmost layer could be domains with the alternating order of 4*f* moments leading to the very small net magnetization. This result indeed becomes a big surprise since then, the spin-texture seen by SR-ARPES is handled via only Rashba effect in the non-centrosymmetric Si-Rh-Si-Tb layer. The results from DFT support this point. Thus, quenched *out of plane* net magnetization opens the way to explore the spin polarization driven solely by the Rashba effect, which is considerably smaller than the exchange interaction in this system (fig. 1c). This is why the respective phenomenon would be hard to explore experimentally for PM phase, since the spin-split of surface state is very small in the Rh- compounds. In AFM phase with the out-of-plane orientation of the magnetization, the strong exchange interaction strongly splits in energy the band of surface state, while the in-plane spin polarization of the later is exclusively handled via the Rashba effect. This effect, which is found to be very different from the well-known classical Rashba effect [3, 4], is a subject of our forthcoming paper.

REFERENCES

1. A. Generalov, et al., Nano Letters **17** 811 (2017).
2. M. Güttler, et al., Scientific Reports **6** 24254 (2016).
3. S.Schulz, et al. npj Quantum Materials **4** 26 (2019).
4. I. A. Nechaev and E. E. Krasovskii, Phys. Rev. B **98**, 245415 (2018).

Spin structure of the gapped Dirac cone of first antiferromagnetic topological insulator MnBi$_2$Te$_4$

I.I. Klimovskikh, S. Filnov, D. Estyunin, A.M. Shikin

[a]Saint Petersburg State Univeristy, Russia, 198504

Keywords: Topological insulators, Dirac cone, antiferromagnetism

A number of remarkable experimental observations and theoretical predictions recently made exploiting the property of antiferromagnetism indicate clearly that antiferromagnetic (AFM) systems can be of great practical importance. As opposed to FM materials, antiferromagnets are robust against external magnetic perturbations and do not produce stray fields.

Moreover, such effects as magnetoresistance, spin torque, and ultrafast dynamics observed in certain AFM systems promise significant advances in spin transfer electronics, spin-orbitronics and spin-caloritronics. At the crossroad of antiferromagnetism and the emerging field of "topotronics", i.e. electronics based on the properties of topologically-nontrivial systems, an AFM topological insulator (AFMTI) arises. The AFMTI surface states are sensitive to the loss of the translational symmetry at surface that can lead to the gap opening. However, there may also be AFMTIs whose certain surfaces break the S symmetry due to magnetism which has been predicted to enable exotic physics like quantized magnetoelectric effect or axion electrodynamics.

This project is devoted to spin-resolved photoemission study of the first antiferromagnetic topological insulator, MnBi2Te4[1] and related similar compounds MnBi4Te7 and MnBi6Te10. Theoretical predictions show the localization of the topologically protected surface states at the natural cleavage plane (0001), which are gapped due to breaking of the TRS, with the value of the gap of ~90 meV. Our SQUID magnetic measurements clearly demonstrate the antiferromagnetic phase of MnBi2Te4 with the Neel temperature of 25 K. The ARPES data (see Fig.1) obviously show the Dirac cone formed by surface states, with the gap at the G point of ~90 meV.
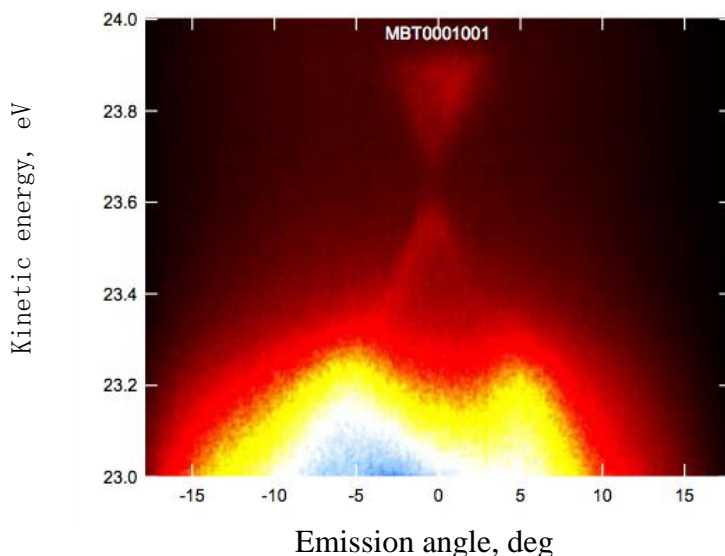
FIGURE 1. ARPES data for MnBi2Te4 taken at G point at a photon energy of 28 eV and temperature of 17 K

By means of spin-resolved ARPES we have studied the spin structure of the Dirac cone of MnBi2Te4, MnBi4Te7 and MnBi6Te10 compounds. Theory predicts the hedgehog spin structure with out-of-plane polarization at the G point of opposite sign for upper and lower cones. Fig.2 presents the spin-resolved ARPES data for the out-of-plane component of spin polarization, taken at G point at the temperature of 17 K. Once can clearly see the spin opposite spin polarization for lower and upper cone, in accordance with the magnetic gap hedgehog spin texture. Our temperature dependent measurements of the spin polarization exhibit the strong changes under antiferromagnetic transition. Moreover, in order to verify the topological character of the formed surface states the in-plane spin polarization components at non-zero wave vector had been studied testifying its helical behavior.
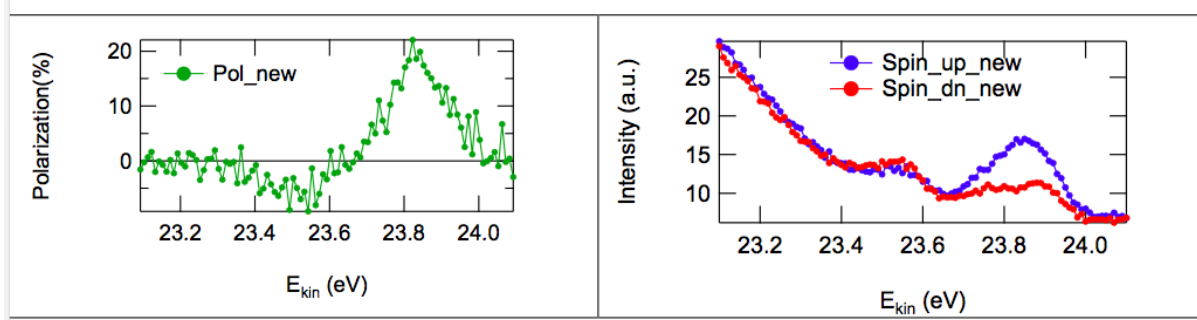
FIGURE 2. Spin-resolved ARPES data for MnBi2Te4 taken at G point at a photon energy of 28 eV and temperature of 17 K. Spin polarization (Spin-up and spin-down spectra) is presented at left (right) panel.

REFERENCES

1. J. Li et al, https://arxiv.org/abs/1808.08608v1 (2018) and D. Zhang et al., https://arxiv.org/abs/1808.08014 (2018) M. Otrokov, I.I. Klimovskikh et al., https://arxiv.org/abs/1809.07389 (2019)
2. R. S. K. Mong, et al., Phys. Rev. B 81, 245209 (2010)
3. T. Hirahara, et al., Nano Letters 17, 3493 (2017)
4. I.I. Klimovskikh, et al., Scientific Reports 7, 3353 (2017)
5. M. Otrokov, et al., 2D Materials 4, 025082 (2017).

Spin-resolved photoemission spectroscopy study
for half-metal Heusler compounds

K Goto[a, b], Y Sakuraba[b], M. Kakoki[c], T. Kono[c], T. Okuda[d] and K Hono[a, b]

[a]*Graduate school of Pure and Applied Science, University of Tsukuba, 1-1-1 Tennodai Tsukuba 305-0047, Japan*
[b]*National Institute for Materials Science, 1-2-1 Sengen, Tsukuba 305-0047, Japan*
[c]*Departmetn of Physical Science, Graduate School of Science, Hiroshima University, 1-3-1 Kagamiyama, Higashi-hiroshima 739-8526, Japan*
[c]*Hiroshima Synchrotron Radiation Center, Hiroshima University, 2-313 Kagamiyama, Higashi-hiroshima 739-0046, Japan*

Keywords: Half-metal Heusler compounds, Spin-resolved ARPES, Temperature dependence of spin polarization

Co-based Heusler compounds such as Co_2MnSi and $Co_2FeGa_{0.5}Ge_{0.5}$ (CFGG) are predicted to have high spin-polarization of the conduction electron at the Fermi level. These materials have been attracting much attention for spintronics devices of tunneling magnetoresistance (TMR) and current perpendicular to plane giant magnetoresistive (CPP-GMR) devices [1-4]. However, observed large reduction of MR ratio with temperature [1, 4] limits a potential of applications using half-metallic Heusler compounds. To understand a cause of this problem, the spin-polarized electronic structure of bulk, surface and interface and its temperature dependence should be observed by spin and angle-resolved photoemission spectroscopy (SARPES) which is the most powerful method for direct measurement of the electronic structure (energy, moment and spin) in the solids.

the CFGG thin film sample which has $L2_1$ structure was prepared by the magnetron sputtering method equipped at National Institute for Materials Science (NIMS) and it was delivered to beam line 9B of Hiroshima Synchrotron Radiation Center (HiSOR) with keeping high vacuum (~3.0×10^{-10} mbar) level by the suitcase chamber. SARPES experiment was performed with a He lamp (hv = 21.2 eV) at the Efficient SPin REsolved SpectroScOpy (ESPRESSO) end station with the very-low-energy-electron-diffraction (VLEED)-type spin polarimeter [5]. Before SARPES measurement, CFGG thin film was annealed at $500℃$ for 30 min to obtain a clean surface. The measurement temperature was room temperature and 45 K.

Figure 1 shows a spin-integrated ARPES image along the $\bar{\Gamma}\bar{X}$ line of CFGG. A parabolic band which crosses Fermi level was clearly observed around 2nd $\bar{\Gamma}$ point. This band crosses Fermi level at $k_{||}$ = 0.86 $Å^{-1}$. To measure the change of the spin polarization with temperature of this band, the SARPES experiment was carried out. Figure 2(a) and 2(b) show the spin-resolved energy distribution curves (EDC) of CFGG measured at 45 K and room temperature, respectively. These EDCs were observed at emission angle of -24°, where $k_{||}$ value is 0.857 $Å^{-1}$. The spin polarization P is estimated from the difference of the photoemission intensity of up spin and down spin. The spin polarization P at Fermi level is 17% at 45 K and it is reduced to 0.7% at room temperature. However, it is unclear that this band is bulk band or surface band. To clarify the origin of the reduction of the spin polarization with temperature, SARPES measurement by using

synchrotron radiation should be performed.

In conclusion, a parabolic band structure which crosses Fermi level was clearly observed around 2nd $\bar{\Gamma}$ point for CFGG thin film. SARPES measurement was performed and the reduction of the spin polarization with temperature at Fermi level was experimentally observed. The spin polarization at Fermi level of the observed parabolic band is 17% at 45 K and it is reduced to 0.7% a room temperature.
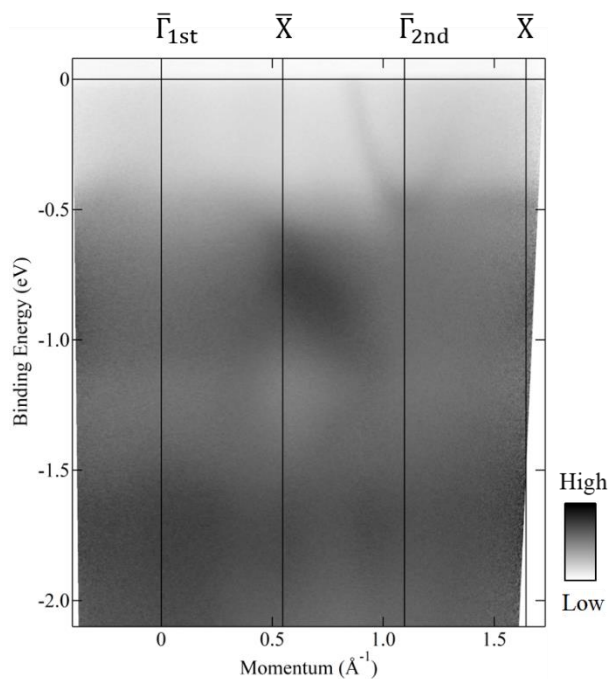
FIGURE 1. Spin integrated ARPES image along the $\bar{\Gamma}\bar{X}$ line of CFGG. The measurement temperature was 40 K.
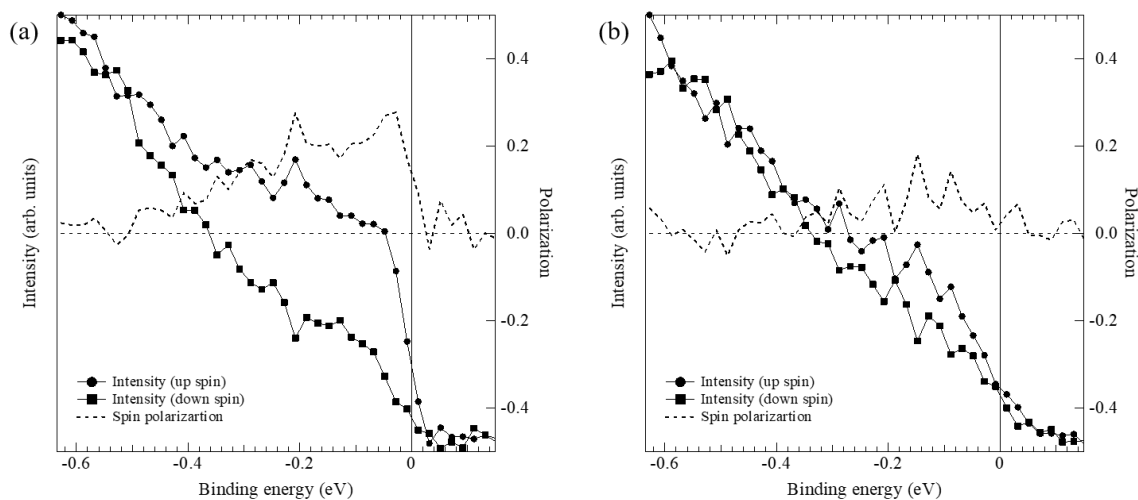
FIGURE 2. Spin resolved EDCs of CFGG at 40 K (a) and room temperature (b). Circles and squares mean the photoemission intensity of up spin and down spin, respectively. The dashed line means the spin polarization.

REFERENCES

1. Y. Sakuraba *et al*., Appl.Phys. Lett. **88**, 192508 (2006)
2. T. Ishikawa *et al*., J. Appl. Phys. **103**, 07A919 (2008)
3. S. Li *et al*., Appl. Phys. Lett. **103**, 042405 (2013)
4. J. W. Jung *et al*., Appl. Phys. Lett. **108**, 102408 (2016)
5. T. Okuda *et al*., Rev. Sci. Instrum. **82**, 103302 (2011)

Identifying sulfur species adsorbed on particulate matters in exhaust gas emitted from a container carrier

Satoshi ASAOKA[a], Tomoshisa DAN[b] and Shinjiro HAYAKAWA[c]

[a] Research Center for Inland Seas, Kobe University,
5-1-1 Fukaeminami, Higashinada, Kobe, 658-0022 JAPAN
[b] Graduate School of Maritime Sciences, Kobe University
5-1-1 Fukaeminami, Higashinada, Kobe, 658-0022 JAPAN
[c] Graduate School of Engineering, Hiroshima University
1-4-1 Kagamiyama, Higashi-Hiroshima 739-8527 JAPAN

Keywords: distillate marine fuel, gas oil, ship diesel engine, sulfonate, sulfate

Particulate matter (PM) from seagoing ships affect the ocean environment on various scales. The estimated annual PM emission from ships is 0.9–1.7 million tons [1]. Because PM and sulfur emission is closely linked to the sulfur content of ship fuels, in 2015 the International Maritime Organization (IMO) introduced regulations that the sulfur content in ship fuel be less than 3.5% and 0.1% for general and designated sea areas, respectively. In 2020, the regulation will be further strengthened to reduce sulfur content in ship fuel to 0.5% for general sea areas [2].

The amount of SOx emitted from seagoing ships has conventionally been estimated by emission factors based on sulfur content in fuels. Although sulfur adsorbed on PM in exhaust gases from fuels is considered to be sulfate, the chemical species of sulfur adsorbed on PM in exhaust gases are not well known, which is an impediment to establishing appropriate regulations for sulfur emission control from ships.

Fig. 1 Sulfur K edge spectra of PM from EMERALD I and sulfate standards
Dotted lines are liner combination fit by the two standards.

The purpose of this study is to identify sulfur species adsorbed on PM or soot emitted from various vessels.

Particulate matter and soot samples were collected from a container carrier, EMERALD I. XAFS analyses of the sulfur K-edge spectra were performed using the BL11 at the Hiroshima Synchrotron Research Center (HiSOR). The sample chamber was filled with He gas. The XAFS spectra were measured in two different modes simultaneously.

The sulfur K-edge spectra of PM collected from the EMERALD I and sulfur and sulfonate standards are shown in **Fig. 1** [3]. The sulfur K-edge spectra of the PM fit well with the combination of sulfate and sulfonate by the linear combination fit. The origin of sulfate and sulfonate in PM is considered to be the oxidation of sulfur substances and sulfide in DMX. The concentration of sulfate and sulfonate adsorbed on PM under 85% load were 19.0 and 1.3 mg m^{-3}, respectively, on the sulfur basis. In the case of 50% load, concentration of sulfate and sulfonate adsorbed on PM were 20.2 and 1.0 mg m^{-3}, respectively, on the sulfur basis. The sulfur species of PM did not show a statistically significant difference between 85% and 50% load.

REFERENCES

1. J. Moldanová, E. Fridell, O. Popovicheva, B. Demirdjian, V. Tishkova, A. Faccinetto, C. Focsa, *Atmos. Environ.* **43**, 2632-2641 (2009)
2. S. Endres, F. Maes, F. Hopkins, K. Houghton, E.M. Mårtensson, J. Oeffner, B. Quack, P. Singh, D. Turner, *Front. Mar. Sci.*, 5, 139 (2018)
3. S. Asaoka, T. Dan., I. Asano, S. Hayakawa, K. Takeda, *Chemosphere*, **223**, 399-405 (2019)

Sulfur K-edge XAFS analysis of aqueous solutions of sulfur compounds using an in-situ liquid flow cell

Daisuke Nishio, Atsuya Doi, Kenji Komaguchi,
and Shinjiro Hayakawa

Department of Applied Chemistry, Graduate School of Engineering, Hiroshima University, Hiroshima, Japan

Keywords: sulfite, XAFS, in-situ liquid flow cell

[Introduction]

There are limited number of analytical methods that provide information on chemical speciation in a solution. UV spectroscopy is widely used because it is highly sensitive, but absorption bands are generally broad and interference of coexisting chemical species often occurs. X-ray Absorption Fine Structure (XAFS) spectroscopy is attractive because of its elemental selectivity, wide applicable range in pH and large probing depth through a solution. Soft X-rays around 3keV cover K-edges of S, Cl, K and Ca and the chemical states of these elements in a solution receive of great interest, and we have developed a sealed cell and a flow cell for XAFS measurements in the soft X-ray region. They are applicable to both transmission and fluorescence modes.

In this presentation outline of the developed flow cell and its application to sulfite solution will be demonstrated. Sulfite has two pKa, and there exist several forms of anions including structural isomers and a dimer depending on pH and the concentration [1,2].

[Experimental]

XAFS measurements were performed on the BL-11 at HiSOR. The beamline is equipped with a Si(111) double crystal monochromator, and K shell spectra from P to Ti are covered. The sample chamber was filled with He gas for minimizing beam attenuation. Intensities of the incident and transmitted beam were monitored with an air filled ionization chamber. Energy scans from 2460 to 2490 eV were carried out to obtain K-edge region of sulfur.

The windows of the cell used were commercial silicon nitride of 1.0μm thick (Norcada) and their opening was 5.0×5.0 mm. The effective cell length was about 300 μm. The cell was placed in the He chamber, and the solution could be circulated from a reserver with a perista pump. A series of measurements were carried out with the system, and the pH was gradually changed (**FIGS 1, 2**). The use of the flow cell was advantageous to maintain the effective cell length constant during the measurements.
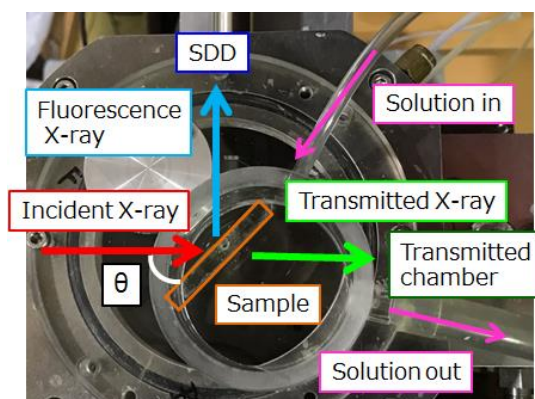
FIGURE1. Sample chamber (top view)
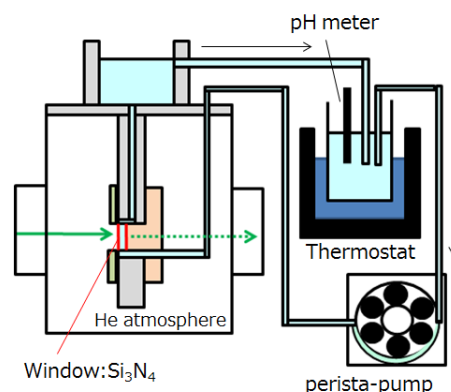
FIGURE2. Schematic layout of flow cell

[Result & Discussion]

FIG. 3 shows XAFS spectra of aqueous 0.1 M Na_2SO_3 solutions as the function of pH. XAFS spectra obtained at pH 10.5, 4.17, and 1.30 were attributed to SO_3^2, HSO_3^-, and SO_2, respectively. HSO_3^- represented structural isomers of $(HO)SO_2^-$ and $(HS)O_3^-$ those have different proton bonding positions

FIG. 4 shows XAFS spectra obtained around pKa_2 (7.19) from solutions of lower (0.1 M) concentration. Isosbestic points appeared, and the solution could be regarded as a binary system within the range of pH. The isosbestic point indicated that the contribution of $S_2O_5^{2-}$ (dimer) was negligible with this concentration and that the XAFS spectra of structural isomers of HSO_3^- could be treated as a single component. The latter result indicated that the fractions of two components were constant within the range of pH or the XAFS spectra of these isomers were almost identical for each other.

The isosbestic point disappeared in XAFS spectra obtained from 1.0 M solutions, and the XAFS spectra were well fitted with the ternary system include contribution of $S_2O_5^{2-}$. An example of the curve fitting was shown in **FIG. 5**. The spectrum was obtained at pH 6.10, and three base spectra were used for fitting. Two of base spectra were that of HSO_3^- obtained at pH 4.17, and that of SO_3^{2-} obtained at pH 9.53, and the rest of the component should be that of $S_2O_5^{2-}$ solution. The spectrum from solid of $Na_2S_2O_5$ was used instead. The resultant portions of three components were 0.58, 0.37 and 0.05 for HSO_3^-, SO_3^{2-} and $S_2O_5^{2-}$, respectively.
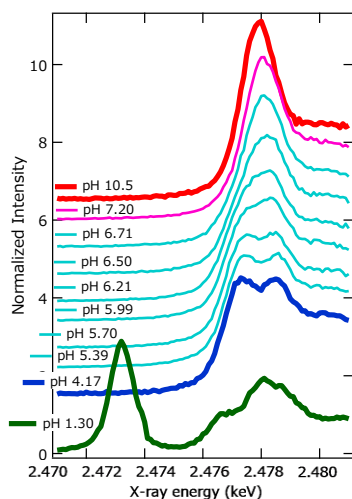
FIGURE3. S K-edge XAFS spectra of 0.1 M Na_2SO_3 solutions as a function of pH.
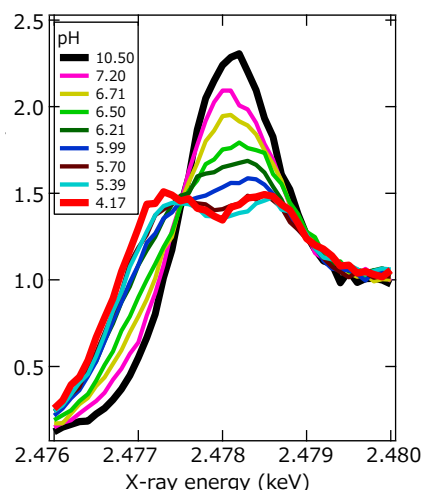
FIGURE4. S K-edge XAFS spectra of 0.1 M Na_2SO_3 solutions around pK_{a2}.
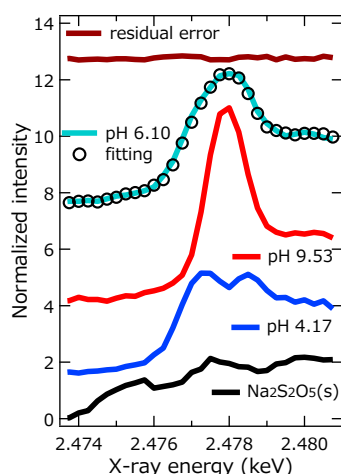
FIGURE5. XAFS spectra obtained at pH 6.10 and the result of curve fitting with three components

[1]D.L. Eldridge *et al.*, *Geochimica et Cosmochimica Acta* **220**, 309–328 (2018)
[2]Yaser Beyad *et al., Dalton Trans.*, **43**, 2147–2152 (2014)

Polarization dependence of S K-edge XAFS spectra from polythiophene thin films

Yuta Hamashima[a], Kohei Fukuda[a], Daisuke Kajiya[b], Ken-ichi Saitow[b], Atsunori Mori[c], Kenji Komaguchi[a], Joji Ohshita[a], Shinjiro Hayakawa[a]

a Department of Applied Chemistry, Graduate School of Engineering, Hiroshima University, Higashi-Hiroshima, Hiroshima, 739-8527, Japan
b Natural Science Center for Basic Research and Development (N-BARD),Hiroshima University, 1-3-1 Kagamiyama, Higashi-hiroshima, Hiroshima, 739-8526, Japan
c Department of Chemical Science and Engineering, Graduate School of Engineering, Kobe University Rokko, Nada, Kobe, 657-8501, Japan

Keywords: XAFS, polythiophene, orientation, uniaxial

1. Introduction

Polythiophene is utilized for various organic electronic devices, and the orientation of polymer thin film affects their performances. Major orientations of planar conjugated backbone are Face-on and Edge-on, and control of the orientation of the film has been thoroughly investigated as a function of molecular weight and solvent [1]. It has also been reported that a uniaxial orientation of Edge-on film can be prepared by substrate treatment [2].

We have developed a method to evaluate the type and fraction of the orientation of polythiophene thin film from the polarization dependence of X-ray absorption fine structure (XAFS).We applied this technique to the quantification of orientation parameters of structurally controlled poly(3-hexylthiophene) (P3HT) thin films.

2. Experimental

P3HT of relatively low molecular weight (Mw = 75,000) was dissolved in o-dichlorobenzene and the other P3HT of relatively high molecular weight (Mw=185,000) was dissolved in chloroform. These solutions were spin-coated on a Si substrate, and they are named as sample A and sample B, respectively. A chlorobenzene solution of P3HT was also prepared and spin-coated on a special ITO/glass substrate, and the surface of the substrate was previously brushed with a velvet fabric (Sample C). In sample C, the backbone of P3HT molecules in Edge-on orientation was aligned along the brushing direction [2].

XAFS measurements were performed at BL-11 of Hiroshima Synchrotron Radiation Center (HiSOR). X-ray fluorescence yield (XFY) was detected with a silicon drift detector (SDD) in a He filled chamber.

Glancing angle dependence of XFY was compared between sample A and B. Glancing angle θ shown in Fig. 1(a) was changed from 20° to 80°. Azimuthal angle dependence of XFY was investigated with-sample C. The azimuthal angle was defined as the angle between the electric field vector and the brushing direction (Fig. 1(b)). The azimuthal angle φ was changed from 0° to 90° by rotating the sample with the glancing angle of 80°.
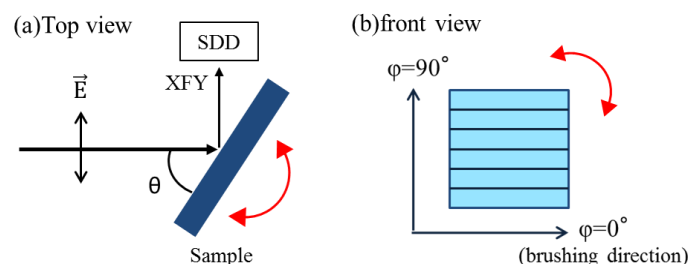
FIGURE 1. The arrangement for (a) glancing angle dependence and (b) azimuthal angle dependence measurement.

Results and Discussion

FIGURE 2 shows the glancing angle dependence of S K-edge XAFS spectra from sample A and sample B. The sample A showed decrease of both σ^*_{S-C} and π^* peaks with the decrease of θ. The result showed that the transition dipole moments from S 1s to σ^*_{S-C} orbital and π^* orbital lay in-plane of the substrate. In sample B, the tendency of π^* peak was opposite to that of σ^*_{S-C} peak, and the result showed that the transition dipole moment to σ^*_{S-C} orbital lay in-plane while that to π^* was perpendicular to the substrate. These anisotropies suggest that P3HT mainly occupied Edge-on orientation in sample A and Face-on orientation in sample B. The ratio of Edge-on orientation to Face-on orientation was calculated to 5.2:1 in sample A, and 1:2.8 in sample B after separating intensities of σ^*_{S-C} peak from π^* peak.
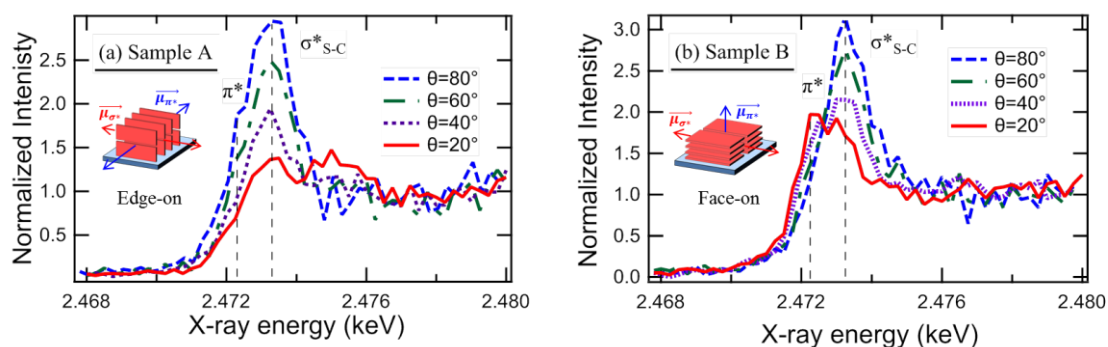
FIGURE 2. Glancing angle dependence of S K-edge XAFS spectra from (a) sample A and (b)sample B.

FIGURE 3 shows the azimuthal angle dependence of S K-edge XAFS spectra from sample C. The σ^*_{S-C} peak appeared strongly under the condition of $\varphi = 0\,°$ because the transition dipole moment to σ^*_{S-C} orbital was mainly parallel to the brushing direction. Plot of the intensities of π^* peak as a function of azimuthal angle is shown in FIGURE 4. They were fitted to the portion similar to $\sin^2\varphi$ curve and the other constant portion. The amplitude of the former portion indicated the quantity of uniaxial oriented Edge-on domain. The rest of the intensity was attributed to those oriented randomly in Edge-on orientation. Approximately 56% of molecules in Edge-on orientation were localized toward brushing direction.

Furthermore, the ratio between uniaxially oriented Edge-on, randomly oriented Edge-on and Face-on orientation was determined to be 2.5:2.0 :2.0 from the azimuthal angle dependence of the intensity of σ^*_{S-C} peak.
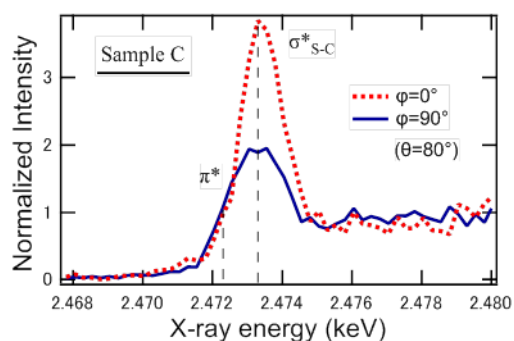
FIGURE 3. Azimuthal angle dependence of S K-edge XAFS spectra from sample C.
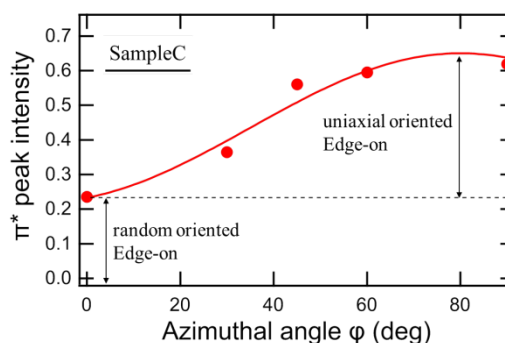
FIGURE 4. Plot of the intensity of π^* peak as a function of azimuthal angle.

References

1. T. Matsumoto, K. Nishi, S. Tamba, M. Kotera, C. Hongo, A. Mori, T. Nishino：*Polymer*.**119**,76 (2017).
2. M. Imanishi, D. Kajiya, T. Koganezawa, K. Saitow: *Sci.Rep*.**7,**5141 (2017).

Identification of sulfur species in road dust collected from emerging countries in Asia

Waqar Azeem JADOON[a], Satoshi ASAOKA[b]

Lawrence LIAO[c] and Shinjiro HAYAKAWA[c]

[a] Graduate School of Biosphere Science, Hiroshima University (1-7-1 Kagamiyama, Higashi-Hiroshima 739-8521 Japan)
[b] Research Center for Inland Seas, Kobe University (5-1-1 Fukaeminami Higashinada Kobe 658-0022 Japan)
[c] Graduate School of Biosphere Science, Hiroshima University (1-4-4 Kagamiyama, Higashi-Hiroshima 739-8528 Japan)
[d] Graduate School of Engineering, Hiroshima University (1-4-1 Kagamiyama, Higashi-Hiroshima 739-8527 Japan)

Keywords: road dust, sulfate, sulfonate, XAFS

In South and East Asia, the rapid development of transportation systems has been linked to the increasing concentration of air pollutants such as particulate matter and road dust. It is therefore necessary to understand sulfur species involved in the temporal and spatial distribution of sulfur-rich particles in order to evaluate human health risks caused by these sulfate-rich particles. The primary goal of this study was to identify sulfur species of road dust collected from emerging countries in Asia.

Road dust samples were collected from roads in rural, sub-urban and urban areas in Afghanistan and Egypt. Sulfur K edge XAFS spectra (ranges 2460–2490 eV) were measured using the BL11 in the Hiroshima Synchrotron Research Center (HiSOR). The synchrotron radiation from a bending magnet was monochromatized with a Si (111) double-crystal monochromator. The sample chamber was filled with He gas. The XAFS spectra were measured by X-ray fluorescence yield (XFY) mode using a SDD detector. The CEY mode obtained spectra of $CuSO_4 \cdot 5H_2O$ were used to calibrate the incident X-ray energy around K edges of sulfur. The K edge main peak of sulfate was set to 2481.6 eV. The road samples were mounted

on a double stick tape (NW-K15; Nichiban) placed in the central hole (15 mm in diameter) of a copper plate. Incident X-ray angle to the sample surface was adjusted to 20 degrees and the X-ray fluorescence was detected from the direction normal to the incident beam in the plane of electron orbit of the storage ring.

The sulfur K-edge spectra of road and sulfur references are shown in Fig. 1. The sulfur K-edge spectra of road dust fit well with the combination of sulfate, sulfonate and cystein by the linear combination fit. The composition of sulfur species ranged 82-88% (Sulfate), 2.8-5.6% (Sulfonate) and 8.2-15% (Cystein), respectively. We considered the sulfate to be derived from the oxidation of sulfur substances in fuel. These organosulfur compounds such as sulfonate and cysteine which represents C-S bound derived from the incomplete combustion of the carbonaceous components in the fuel. The sulfonate might have been derived from fuel because sulfonate is one of the major components in sulfur species in petroleum, or from the oxidation of sulfide in fuel.
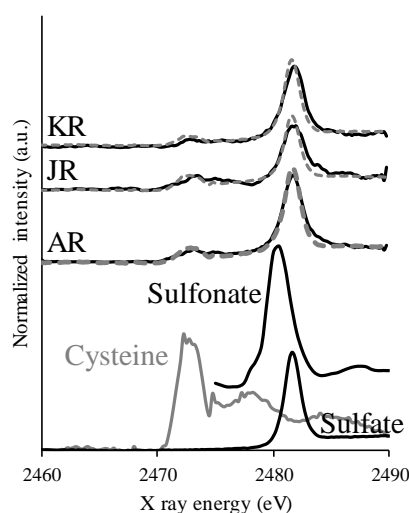
Figure. 1 Sulfur K edge spectra of road dust
Dotted lines are liner combination fit by the three standards.
KR: Kabul in Afghanistan
JR: Jalalabad in Afghanistan
AR: Alexandria

Efficient photocatalytic activation of C-H bonds by spatially controlled chlorine and titanium on the silicate layer

Nao Tsunoji,[a] Hidechika Nishida,[a] Kenji Komaguchi, Shinjiro Hayakawa,[a] Yuya Yagenji,[a] Masahiro Sadakane,[a] and Tsuneji Sano[a]

[a] *Department of Applied Chemistry Graduate School of Engineering, Hiroshima University,*

Keywords: `photocatalysis` • tianosilicate • layered silicate • cyclohexane • selective oxidation • C-H activation

The efficient activation and transformation of $C(sp^3)$-H bonds in alkanes to produce higher-value products remains one of the biggest challenges in modern chemistry. Such bonds are thermodynamically strong and kinetically inert, and molecular oxygen is an unreactive oxidant. Therefore, traditional catalytic strategies for their conversion require the use of expensive and aggressive reagents and/or severe reaction condition. Heterogeneous photocatalysis has become regarded as a promising alternative strategy in recent years since it can be used to activate stable alkanes, even in mild conditions, using solar energy directly. Nonetheless, as the lack of efficient photocatalysts for scale-up production of target organics remains the bottleneck for industrialization, more precise catalyst design strategies that can efficiently harness photons for organic transformations are highly desirable.

In the current study, we selected two inorganic elements (chlorine and titanium) and developed highly efficient photodriven organic transformations by accurate control of their spatial distribution.[1] Recently, Yuan et al. reported that chlorine radicals generated on the surface of a titanium-oxide-based photocatalyst can activate primary hydrocarbons and effectively produce partially oxidized products.[2] The authors proposed that chemisorbed chlorine is trapped by photogenerated holes to produce chlorine radicals. The specific radical generates alkyl radicals that can subsequently yield partially oxidized organics through reactions with molecular oxygen. However, in this system, over-oxidation can proceed through the consumption of electron-hole pairs by

FIGURE 1. HUS-7 silicate framework viewed along the (a) c-axis, (b) b-axis, and (c) a-axis. The dotted squares indicate the repeating structural unit containing a silanol and a silanolate group. (d) Ti grafting and chlorination on the HUS-7silicate layer.

molecular oxygen and the hydrocarbon, resulting in low catalytic efficiency for the partially oxidized product. Therefore, the specific radical mediator (chlorine) should be located at a position neighboring the photoexcitation center to ensure more efficient electron transfer between them.

Recently, we developed a rational design strategy for realizing isolated metal species on layered silicates. Layered silicates composed of anionic silicate sheets with interlayer cations are a kind of layered material whose interlayer surfaces are covered with silanol (SiOH) and silanolate (SiO⁻) groups with crystallographically defined arrangements and bond angles.[3-6] We found that isolated titanium species with uniformly tetrahedral coordination states and high surface densities are provided by the grafting of titanium(IV) acetylacetonate onto the surface of a Hiroshima University silicate (HUS, Figure 1). As shown in Figure 1, further remarkable features of this material are the specific coordination environment of isolated species linked by two Ti−O−Si bridges and the presence of exchangeable ligands (acetylacetonate or hydroxyl groups). In this study, we attempted to incorporate chlorine at locations neighboring isolated

titanium atoms by ligand exchange, yielding a chlorinated layered silicate catalyst. The C-H activation ability of the catalyst was evaluated in the photocatalytic oxidation of cyclohexane into its partially oxidized products cyclohexanone and cyclohexanol, which are important intermediates in the manufacture of nylon polymers. We also employed a chlorine-incorporating zeolite material (TS-1) and titanium oxide (P25) for comparison in order to assess the influence of the spatial distribution of the elements on the efficiency of the partial oxidation reaction.

To investigate the coordination environments in Ti-HUS and TS-1, K-edge X-ray absorption spectroscopy (XAS) measurement of titanium and chlorine was performed (Figure 2). The titanium K-edge for TS-1 presents a very sharp pre-edge peak at an energy of approximately 4,968 eV, attributable to transitions from the 1s to the 3d level in isolated titanium atoms surrounded by four oxygen atoms. In contrast, although the pre-edge peak is broadened in the layered silicate sample, there is hardly any change in the XANES spectrum upon chlorination. This confirms that chlorination does not affect the coordination environment of the titanium atoms in either sample. The broad pre-edge for Ti-HUS could possibly result from the asymmetric coordination environment of titanium, which is composed of organic (acac) and inorganic (SiO) ligands. A similar broadening of the pre-edge peak was also observed in a previous study of titanium-complex immobilization on layered silicate. For the Cl K-edge, no difference in the spectra of the chlorinated zeolite and layered silicate is observed. The spectra show a very broad second absorption at ≈2,840 eV below the broad main absorption at 2,826 eV composed of two partially resolved peaks. A similar trend in the XANES spectra has been observed for Cl anions in aqueous solution.[6] Considering the differences in titanium coordination state between TS-1 and Ti-HUS as well as the loss of organic ligands in Ti-HUS upon chlorination, it appears that the organic ligands on the silicate-immobilized titanium are first exchanged for chlorine. Then, hydration occurs due to the low water resistance of Ti-Cl bonds, resulting in chlorine existing as a hydrated HCl in both samples.

The chlorinated layered silicate photocatalyst exhibited a remarkably high production rate (0.7 mmol g^{-1} h^{-1}) and large amount of product formed (0.8 mmol), while the over-oxidation of cyclohexane was inhibited. This excellent activity and selectivity is explained by the presence of a radical mediator (chlorine) located at a position neighboring an isolated titanium atom. The high surface density of these active species on the silicate layer provides efficient electron transfer to form chlorine radicals.
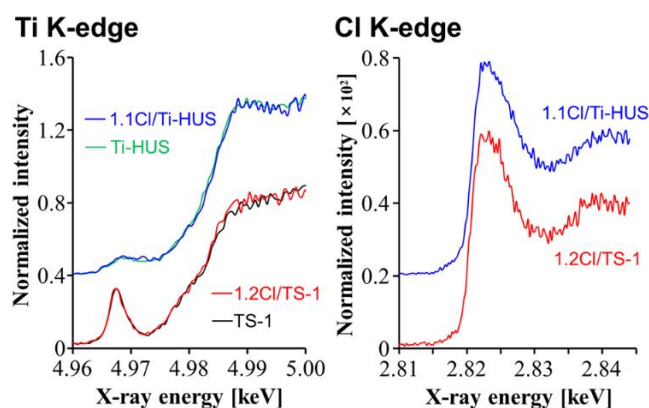
FIGURE 2. (left) Ti and (right) Cl k-edge XANES spectra for TS-1 and Ti-HUS before and after Cl incorporation.

REFERENCES

1. N. Tsunoji, H. Nishida, Y. Ide, K. Komaguchi, S. Hayakawa, Y. Yagenji, M. Sadakane, T. Sano, *ACS Catal.* **2019**, *9*, 5742-5751.
2. R. Yuan, S. Fan, H. Zhou, Z. Ding, S. Lin, Z. Zhang, C. Xu, L. Wu, X. Wang, X. Fu, *Angew. Chem. Int. Ed.* **2013**, *125*, 1069-1073.
3. N. Tsunoji, T. Ikeda, M. Sadakane, T. Sano, *J. Mater. Chem. A* **2014**, *2*, 3372-3380.
4. N. Tsunoji, Y. Ide, Y. Yagenji, M. Sadakane, T. Sano, *ACS Appl. Mater. Interfaces* **2014**, *6*, 4616-4621.
5. N. Tsunoji, M. Bandyopadhyay, Y. Yagenji, H. Nishida, M. Sadakane, T. Sano, *Dalton Trans.* **2017**, *46*, 7441-7450.
6. N. Tsunoji, M. V. Opanasenko, M. Kubu, J. Cejka, H. Nishida, S. Hayakawa, Y. Ide, M. Sadakane, T. Sano, *ChemCatChem.* **2019**, *9*, 5742-5751.

Conformation Analysis of Chitin by Vacuum-Ultraviolet Circular Dichroism Spectroscopy

Koichi Matsuo

Hiroshima Synchrotron Radiation Center, Hiroshima University,
2-313 Kagamiyama, Higashi-Hiroshima, Hiroshima 739-0046, Japan

Saccharides has various biological functions such as the molecular recognition between cell and virus and the protections of biomolecules from cold and dry conditions. However, the characterizations of these conformations are often difficult because they take a complicated equilibrium state in aqueous solution. Vacuum-ultraviolet circular dichroism (VUVCD) spectroscopy can extend the CD measurements down to 140 nm and can be used for detecting the saccharide structures in aqueous solution because the CD spectra sensitively reflect the structural characteristics such as the types of glycosidic linkages of di-saccharides [1, 2]. Previously, we measured the VUVCD spectra of malto-, isomalto-, cello-, and laminari-oligosaccharides (all of constituent mono-saccharides are D-glucose) with various chain length, and clearly observed the folding process of the helical structure of oligomers accompanied with the increment of the chain length [3]. In the present study, the conformation study of oligosaccharides was extended to chitin (glycosaminoglycans) [4] which is composed of *N*-acetylglucosamine (NAG) (See the chemical structure shown in Figure 1).

The VUVCD spectra of five types of β-(1→4) linked NAG oligomers with the degree of polymerization (DP) from 2 to 6 were measured from 200 to 170 nm at 25°C in aqueous solutions. The VUVCD spectrum of chitin_DP2 showed one negative peak around 210 nm, one positive peak around 190 nm, and negative sign at 170 nm. Previous study showed that the spectrum of NAG had one negative peak around 210 nm and one positive peak around 180 nm [4]. From the differences between NAG and chitin_DP2, it is suggested that the effect of β-(1→4)-glycosidic linkage to CD exhibits below 190 nm. Chitin_DP3 exhibited similar spectrum with that of DP2 but the positive peak around 190 nm was slightly red-shifted. The chitin_DP3 and DP4 showed mostly same spectral shape. On the other hand, the spectral shape of chitin_DP5 and DP4 showed slight difference below 200 nm, although the DP5 and DP6 had similar spectra again. These results suggest that the spectra of chitin changed step by step with the increment of DP. The CD study of malto- and laminari-oligosaccharides indicated that the spectral change depending on the chain length between 200 to 180 nm was affected by the formation of regular structure of oligosaccharide [3]. These results mean that the chain-dependence of CD observed in this study might relate to the formation of unique structure of chitin.
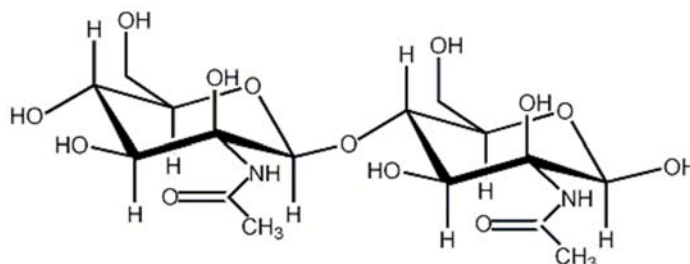
Figure 1. Chemical structure of chitin (DP=2).

References
1. R. G. Nelson and W. C. Johnson, *J. Am. Chem. Soc.* **94**, 3343-3345 (1972).
2. K. Matsuo and K. Gekko, *Carbohydr. Res*. **339**, 591-597 (2004).
3. K. Matsuo, *Biomed. Spectrosc. Imaging* **6** 111-121 (2017).
4. K. Matsuo, H. Namatame, M. Taniguchi, K. Gekko, *Biosci. Biotech. Biochem.* **73**, 557-561 (2009).

Structural change of DNA repair protein XRCC4

by phosphorylation at c-terminal revealed by VUV-CD

Kai Nishikubo[a,b], Maho Hasegawa[a], Yudai Izumi[c], Kentaro Fujii[b],
Koichi Matsuo[c], Yoshihisa Matsumoto[d], Akinari Yokoya[b]

[a]*Graduate School of Science and Engineering, Ibaraki University, Japan*
[b]*Quantum Beam Science Research Directorate, National Institutes for Quantum and
Radiological Science and Technology (QST), Japan*
[c]*Hiroshima Synchrotron Radiation Center, Hiroshima University, Japan*
[d]*Tokyo Institute of Technology*

Keywords: XRCC4, vacuum ultraviolet circular dichroism

XRCC4 is activated via phosphorylation of its several sites by DNA-PK in the DNA double strand break repair pathway (NHEJ) (1). The phosphorylation might cause a change of static electric charge at the amino acid residues, resulting conformational alteration of the whole protein structure to permit the protein accessibility to the strand break terminus through the charge re-distribution in the protein. In order to understand the role of XRCC4 properly, it would be necessary to understand the mutual relationship between its structural change and activity change. So far, the crystallography of XRCC4 has been performed, but there is no data on the full-length of XRCC4 because it is difficult to crystallize 130 amino acid residues in the C-terminal which including several targets of phosphorylation. Instead of crystallography, we have applied circular dichroism (CD) spectral analysis for XRCC4 in an aqueous solution in a vacuum UV region at HiSOR. When compared the content of the secondary structures obtained by the CD measurement of the intact XRCC4 (denoted as WT) with that reported in the previous crystallography, the non-crystalized C-terminal region was revealed to contain significant turn structures, but not to contain β-strand. A mutated XRCC4, in which the serine-320 was substituted to an aspartic acid (denoted as S320D) to mimic phosphorylation, was also analyzed. The content of β-strand of S320D was slightly less than that of WT. The evidences indicate that β-strand in the N-terminal region was affected despite the substitution with aspartic acid induced at the C-terminal region. The phosphorylation of C-terminal region would play a role to regulate the activity of the protein through altering its whole structure, including the active center in the N-terminal.

Figure 1 shows VUV-CD spectra of full-length XRCC4WT and XRCC4S320D. A positive peak at 190 nm and negative peak at around 208 nm are the characteristic CD peaks of α-helix structures (2).
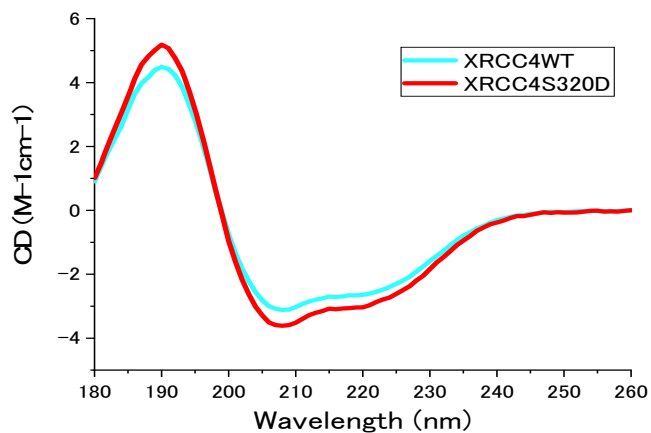
FIGURE 1. VUV-CD spectra of full-length XRCC4 in an aqueous solution.

TABLE 1. Secondary structural contents of XRCC4

	1FU1(3)	WT	S320D
length (residues)	203	342	342
α−helix (%)	38	34.3	37.4
β−strand(%)	26	15.3	13.2
turn (%)	8	22.8	22.4
random (%)	28	27.5	26.9

In table 1, 1FU1 is previously reported from crystallography (3). WT and S320D are the result of CD measurement at HiSOR.

REFERENCES

1. Kamdar,R.P. and Matsumoto,Y. Radiation-induced XRCC4 Association with Chromatin DNA Analyzed by Biochemical Fractionation. J.Radiat.Res 2010; 51, 303-313.

2. Matsuo.K. Structural analysis of protein using synchrotron radiation vacuum-ultraviolet circular dichroism. The Journal of Biochemistry 2004 135,3, p. 405-411.

3. Junop, M.S., Modesti, M., Guarne, A., Ghirlando, R., Gellert, M., Yang, W. Crystal structure of the Xrcc4 DNA repair protein and implications for end joining. EMBO J 2010. 19: 5962-5970.

Circular Dichroism Analysis of Optical Activity Emergence in Amino-acid Thin Films Irradiated by Vacuum-ultraviolet Circularly-polarized Light

Jun-ichi Takahashi[a], Toshiki Sakamato[a], Yudai Izumi[b], Koichi Matsuo[b]
Masaki Fujimoto[c], Masahiro Katoh[c], Yoko Kebukawa[a], Kensei Kobayashi[a]

[a]*Faculty of Engineering, Yokohama National University, 79-5 Tokiwadai, Hodogaya-ku, Yokohama 240-8501, Japan*
[b]*Hiroshima Synchrotron Radiation Center, Hiroshima University, 2-313 Kagamiyama, Higashi-Hiroshima 739-0046, Japan*
[c]*UVSOR Facility, Institute for Molecular Science, 38 Nishigo-Naka, Myodaiji, Okazaki 444-8585, Japan*

Keywords: Homochirality, Amino Acid, Optical Activity, Circularly-polarized Light, Circular Dichroism

The origin of homochirality in terrestrial bioorganic compounds (L-amino acid and D-sugar dominant) remains one of the most mysterious problems in the research for the origins of life. Rational explanations for the chiral asymmetry introduction of into bioorganic compounds are required because organic compounds synthesized in abiotic environments are intrinsically racemic mixtures (equal amounts of L- and D-bodies). One of the most attractive hypotheses in the context of astrobiology is "Cosmic Scenario" as below;

(1) Asymmetric reactions of prebiotic molecules adsorbed on interstellar dust surfaces in molecular cloud circumstances were introduced by asymmetric radiation sources in space, that is "chiral radiations". (2) The chiral products were transformed into the complex organic materials including amino-acid precursors as "chiral seeds". (3) The complex organic materials as "chiral seeds" were transported with meteorites or asteroids to primitive Earth resulting in terrestrial biological homochirality [1].

Eventually, wide radiation regions of circularly-polarized light (CPL) in space originated by light scattering from interstellar dusts in star formation regions have been observed by telescopic infrared polarization analysis. These observations have indicated that CPL is one of the potential candidates for "chiral radiations" sustaining the credibility of Cosmic Scenario [2].

In addition to observations, several ground experiments to validate the scenario have been investigated asymmetric photochemical reactions in simple biochemical molecules using CPL radiation from high-energy particle accelerators. We have reported optical activity emergence in solid-phase films of racemic amino acids by left- or right-handed CPL (L- or R-CPL) irradiation of 215 nm in wavelength from free electron laser (FEL) of UVSOR-II [3]. By analysis using conventional circular dichroism (CD) spectrometer, preferential structural changes between the two enantiomers in racemic amino-acid mixtures have been introduced by L- or R-CPL irradiation.

As mentioned above, CD spectroscopy can detect optical activity emergence with a high accuracy because CD spectra sensitively reflects the steric structures of chiral molecules. The theoretical calculation of CD spectrum of L-alanine molecule has revealed that the chromophores such as carboxyl and amino groups are derived from characteristic electronic transitions (n-π*, π-π*, and n-σ*) corresponding to different wavelengths below 230 nm [4], suggesting that optical activity emergence by asymmetric photochemical reactions depends on the irradiation wavelength.

In present, we are carrying out irradiation experiments of different CPL wavelengths at an undulator beam line BL1U of UVSOR-III. As for the sample, we formed thin solid films of racemic mixture of alanine on quartz substrates from crystal powders of DL-alanine (L/D = 50/50) as a sublimation source by using a thermal-crucible vacuum-evaporation system in Hiroshima Synchrotron Radiation Center (HiSOR). Sublimation temperature was controlled in the range of 150~200°C and pressure of the vacuum chamber was approximately 5×10^{-2} Pa throughout the evaporation process. The CD spectra of thin solid films just

after the deposition were measured from 260 to 160 nm in wavelength using a vacuum-ultraviolet (VUV) CD instrument at beam line BL-12 of HiSOR and confirmed to be mostly zero CD before the irradiation, showing that the spurious CD due to the contamination of film surface were negligible.

The thin solid films of racemic mixture of alanine were irradiated of L- or R-CPL in different wavelengths using the undulator beam line BL1U of UVSOR-III [5]. In case of CPL irradiation in shorter wavelengths than 200 nm, the samples were set in a vacuum sample chamber preventing attenuation by air absorption [6]. On the beam entrance side of the vacuum sample chamber, a gate valve with a vacuum-sealed MgF_2 or LiF window was mounted. The irradiated CPL wavelengths were 180 and 155 nm corresponding to photon absorption bands of alanine molecule [7]. The irradiated photon energy dose was measured with photoelectron current of a silicon photodiode (International Radiation Detectors, Inc.) settled at the sample position. The typical energy dose calibrated by using quantum efficiency data of the silicon photodiode was approximately 30~60 mWhour.

CD spectra of the CPL irradiated films were measured at beam line BL-12 of HiSOR to clarify the optical activity emergence by CPL irradiation. In order to delete the effects of linear dichroism (LD) and/or linear birefringence (LB) components, dependence on sample rotation angle (0, 45, 90, and 135 degrees) of the CD spectra was measured. The observed spectral profile strongly depends on the irradiated CPL wavelength and the polarization (L- or R-CPL). In Fig.1, CD spectra of DL-alanine films irradiated by L- or R-CPL at 180 or 155 nm in wavelength are shown. Detailed analysis of CD spectra are in progress to clarify full mechanism of the optical activity emergence, which potentially has relevance to the origin of terrestrial bioorganic homochirality stimulated by "chiral radiation".

(a) **(b)**
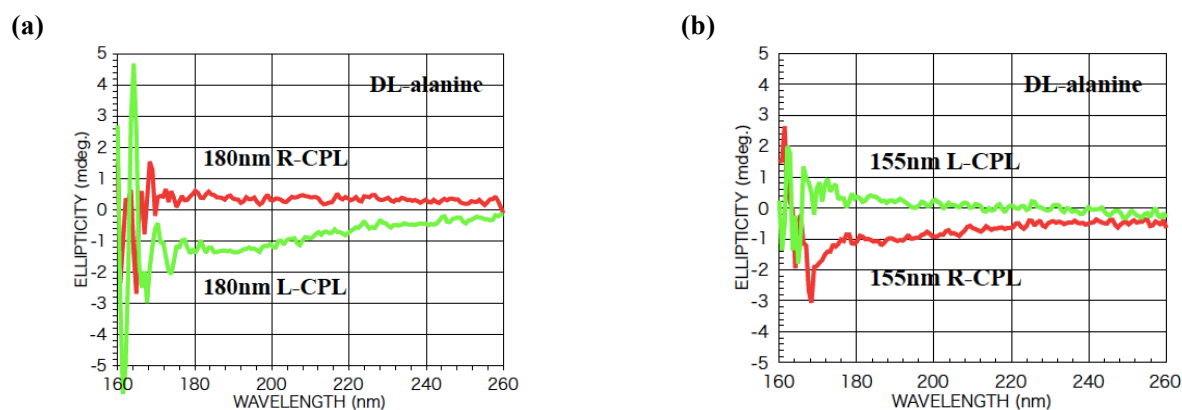
FIGURE 1. CD spectra of the L- or R-CPL irradiated DL-alanine film measured at BL-12 of HiSOR. The CPL irradiation wavelengths were (a) 180 nm and (b) 155 nm at BL1U of UVSOR-III.

REFERENCES

1. W. A. Bonner, *Orig. Life Evol. Biosph.* **21,** 407 (1991).
2. T. Fukue et al., *Orig. Life Evol. Biosph.* **40,** 335 (2010).
3. J. Takahashi et al., *Int. J. Mol. Sci.* **10,** 3044 (2009).
4. T. Fukuyama et al., *J Phys. Chem.* **A109**, 6928 (2005).
5. K. Matsuo et al., *UVSOR Activity Report 2016* **44**, 157 (2017).
6. J. Takahashi et al., *HiSOR Activity Report 2017*, 126 (2018).
7. F.Kaneko et al., *J. Phys. Soc. Jpn.* **78** 013001 (2009).

VUVCD Measurement of Lysine-36 Trimethylated Histone H3 protein (H3K36me3)

Yudai Izumi and Koichi Matsuo

aHiroshima Synchrotron Radiation Center, Hiroshima University, Japan

Keywords: Post-translational modification, epigenetics

   Post-translational methylation and demethylation of histone H3 proteins have been reported to play substantial roles in cellular functions. For example, it is known that trimethylation of H3 on the lysine-36 (K36) residue links to DNA damage repair [1]. The conformation of protein closely relates to its biological function, and hence the structures of (un)methylated H3 proteins would be important factors for understanding the roles in the cellular functions. In this work, the CD spectrum of K36 trimethylated H3 (H3K36me3), which is recognized as one of the important methylated H3 proteins, was measured in order to predict the positions of α-helix and β-strand structures of the protein [2].

   Recombinant *Xenopus laevis* H3K36me3 protein was purchased from Active Motif. The reagent was dissolved with 25 mM sodium phosphate buffer supplemented with 250 mM sodium fluoride (pH 8.6 at 25°C). Final concentration of H3K36me3 was 1 mg/ml. CD spectroscopy was carried out in the BL12 beamline at the Hiroshima Synchrotron Radiation Center in Japan. The secondary-structure sequence was predicted using neural-network method based on CD spectroscopic results [3].

   Figure 1 shows the CD spectra of H3K36me3 and unmethylated H3. The CD spectrum of unmethylated H3 was reproduced from Ref. [4]. Both spectra show a positive peak around 190 nm and negative peaks around 200-230 nm. However, the spectral shapes differed from each other. CD spectral shapes reflect the secondary structure contents of proteins, which means that trimethylation of K36 residue induced the structural alterations of H3.
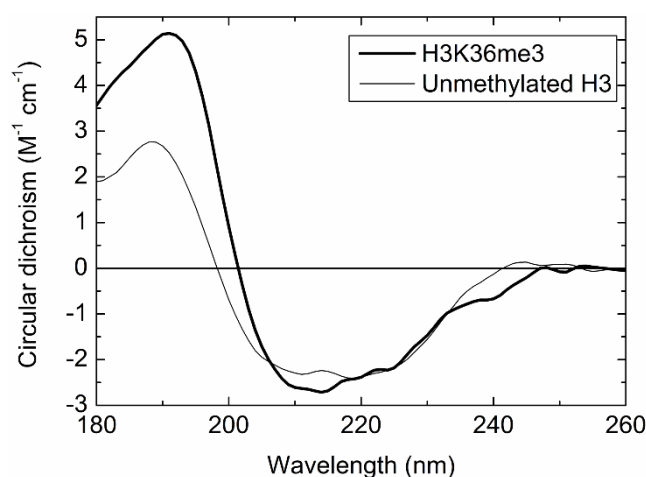
Fig. 1. CD spectra of H3K36me3 (thick line) and unmethylated H3 (thin line) [4].

   Figure 2 shows predicted secondary structure sequence of H3K36me3 and unmethylated H3. It was predicted that the structural alterations were not limited to the regions around methylation site. For example, α-helix formations induced by K36 trimethylation were predicted at the 14th–17th, 77th–82nd, and 85th–86th residues. Similarly, β-strand formation was also predicted at 36th–42nd residues. On the other hand, the α-helix and β-strand structures at the 122nd–130th residues changed to other structures, namely turn and/or unordered structures.

   The structural alteration induced by K36 trimethylation differed from those induced by mono-, di-, or

trimethylation of lysine-4 or -9 residues [4, 5]. These results suggest that the structural changes induced by post-translational methylation are not uniform, but are rich in variation depending on the sites of methylation and methylation degree. The various structural alterations may be strongly related to the regulation of cellular functions, such as DNA repair pathway.
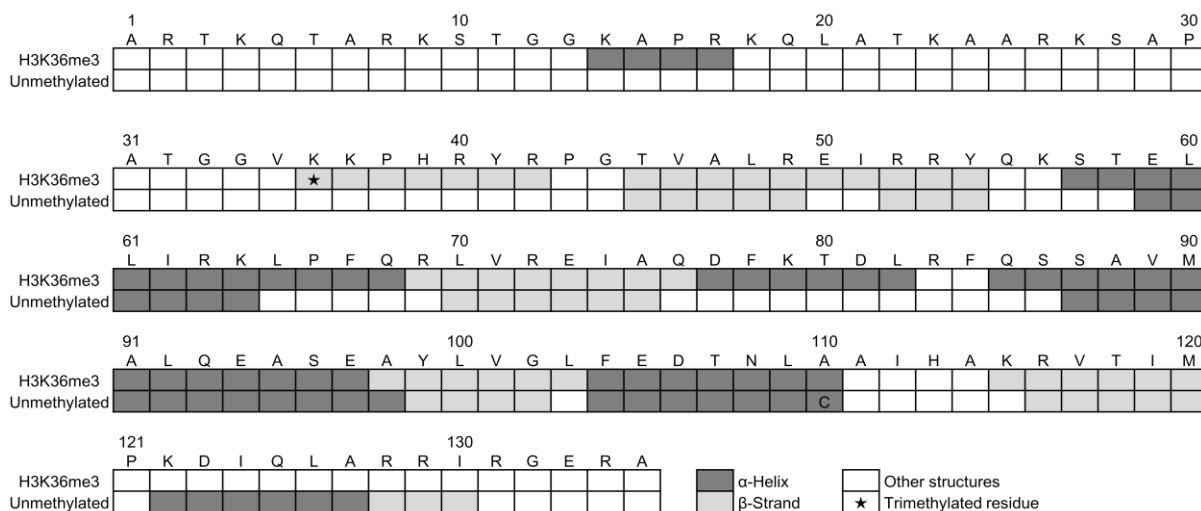
Fig. 2. Sequence-based secondary structures of H3K36me3 and unmethylated H3. The positions predicted formation of α-helix, β-strand, and other structures are colored in gray, light gray, and white, respectively. The mark ★ in the rectangle represents methylated site. The data of unmethylated H3 was reproduced from Ref. [4]. The 110th residue of unmethylated H3 reagent is cysteine (C) which is different from that of the H3K36me3 reagent.

References
[1] T. Clouaire and G. Legube, *Nucleus* **6**, 107-113 (2015).
[2] Y. Izumi and K. Matsuo, *Molecules* **23**, 2865 (2018).
[3] K. Matsuo *et al.*, *Proteins* **73**, 104-112 (2008).
[4] Y. Izumi *et al.*, *J. Radiat. Res.* **59**, 108-115 (2018).
[5] Y. Izumi *et al.*, *Chirality* **30**, 536-540 (2018).

Study on Structural Changes of Histone Core Proteins in *Arabidopsis* after Gamma Irradiation

Jin-Hong Kim[a,*], Tae Ho Ryu[a], and Yudai Izumi[b]

aAdvanced Radiation Technology Institute, Korea Atomic Energy Research Institute, 29 Geumgu-gil, Jeongeup-si, Jeollabuk-do 56212, Republic of Korea
bHiroshima Synchrotron Radiation Center, Hiroshima University,2-313 Kagamiyama, Higashi-Hiroshima, Hiroshima 739-0046, Japan

Keywords: histone modification, chromatin remodeling, DNA damage response, Arabidopsis thaliana, circular dichroism.

SWITCH/SUCROSE NONFERMENTING (SWI/SNF) chromatin remodeling proteins play essential roles in diverse biological processes including DNA repair and apoptosis [1]. The DECREASE IN DNA METHYLATION1 (DDM1), a plant-specific SWI2/SNF2-like chromatin remodeler, is necessary for DNA methylation and heterochromatin maintenance in *Arabidopsis thaliana* [2, 3]. We found that the *ddm1-2* mutant, which has a defect in the helicase domain of DDM1, is more sensitive than the wild type (WT) in response to gamma irradiation. However, the radiation-sensitive phenotype was complemented by overexpressing the intact DDM1 in the *ddm1* mutant. Therefore, the comparative analysis of chromatin structure in the *ddm1-2* and *DDM1-OE/ddm1-2* lines is important in elucidating the mechanism of DDM1-mediated chromatin remodeling in response to gamma irradiation. This study aimed to elucidate the structural changes of core histone proteins in chromatin after gamma irradiation, which can be associated with the differential DNA damage responses in the WT, *ddm1-2* and *DDM1-OE/ddm1-2* lines.

The sterilized *A. thaliana* seeds were stratified at 4°C for 2 days and germinated in 1/2 MS medium supplied with 1% sucrose and 0.65% agar. The 14-day-old seedlings were exposed to gamma radiation with a dose of 200 Gy (50 Gy/hr) using a ^{60}Co source (42.6 TBq, AECL, Canada) at Korea Atomic Energy Research Institute) at room temperature. Core histone proteins were extracted using the Histone Purification Kit (Active Motif Inc., Carlsbad, CA) as described by Izumi *et al.* [4] with some modifications. The extracted proteins were lyophilized using a freeze dryer (FreezeMobile 25EL, SP Scientific, Warminster, PA) and stored at room temperature until use. For VUVCD analysis, the lyophilized samples were dissolved with 10 mM Tris-HCl and 250 mM NaF to induce higher-order structures of histone proteins.

The circular dichroism (CD) intensities obtained as ellipticity θ in millidegrees were converted to molar CD $\Delta\varepsilon$ (M^{-1} cm^{-1}) to compare them. Molar CD is approximately described as

$$\Delta\varepsilon = \frac{\theta\, MRW}{32980\, c\, L},$$

where MRW, *c*, and *L* are residue weight, concentration of the sample (mg/ml), and path length (0.0050 cm), respectively. In this analysis, we defined MRW as follows.

$$MRW = \frac{2*(14000 + 13900 + 15400 + 11400)}{2*(129 + 125 + 135 + 102)} = 111.4.$$

In the CD spectra analysis, the WT, *ddm1-2* and *DDM1-OE/ddm1-2* showed substantially different CD spectra of core histone proteins before and after gamma irradiation (Fig. 1). However, the difference in CD spectra between the CT and GR samples was much more conspicuous in the *ddm1-2* than in the WT and *DDM1-OE/ddm1-2*.
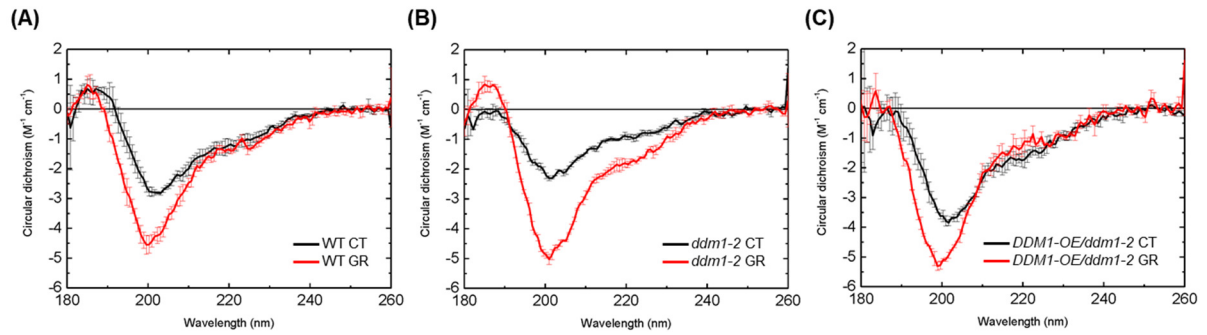
FIGURE 1. CD spectra of core histone proteins in WT, *ddm1-2*, and *DDM1-OE/ddm1-2* plants. CT, control; and GR, gamma ray. All values are average ± S.D. (n = 2 or 3).

Secondary structure contents of core histone proteins were calculated using the SELCON3 program from the CD spectra, based on the reference data measured at HiSOR [4]. The content of α-helix was noticeably increased in the *ddm1-2* but decreased in the *DDM1-OE/ddm1-2*, whilst that of β-strand showed the reverse trend between the two lines. The unordered secondary structures were commonly increased. These results suggest that DDM1 may function in chromatin remodeling required for DDR in plants.

TABLE 1. Secondary structure contents of core histone proteins in WT, *ddm1-2*, *DDM1-OE/ddm1-2* plants. CT, control; and GR, gamma-irradiated. All values are average ± S.D. (n = 2 or 3). Unit: %.

	α-Helix	β-Strand	Turn	Unordered
WT CT	11.9 ± 2.1	31.3 ± 1.7	21.2 ± 0.5	35.6 ± 1.2
WT GR	11.5 ± 2.1	25.6 ± 2.3	21.2 ± 1.0	41.7 ± 0.9
ddm1-2 CT	10.3 ± 0.6	30.0 ± 1.4	23.2 ± 0.3	36.7 ± 1.0
ddm1-2 GR	14.7 ± 0.6	21.3 ± 1.0	21.5 ± 0.3	42.5 ± 1.4
DDM1-OE/ddm1-2 CT	14.1 ± 1.6	22.7 ± 3.2	22.3 ± 1.1	41.0 ± 1.4
DDM1-OE/ddm1-2 GR	7.8 ± 1.1	24.3 ± 2.0	21.5 ± 1.1	46.5 ± 0.8

In conclusion, this study demonstrates that DDM1, a SWI/SNF chromatin remodeling protein, is involved in radiation sensitivity of plants by affecting the structural changes of core histone proteins and chromatin remodeling in response to gamma radiation. In the further study, the functional roles of IR-induced structural changes of core histone proteins will be explored in association with DNA damage responses.

REFERENCES

1. J-H. Park, E-J. Park, S-K. Hur, S. Kim and J. Kwon, Mammalian SWI/SNF chromatin remodeling complexes are required to prevent apoptosis after DNA damage, *DNA Repair* **8**, 29-39 (2009).
2. T. Kanno, W. Aufsatz, E. Jaligot, M. F. Mette, M. Matzke and A. J. Matzke, A SNF2-like protein facilitates dynamic control of DNA methylation, *EMBO Rep.* **6**, 649-655 (2005).
3. A. Zemach, M.Y. Kim, P.-H. Hsieh, D. Coleman-Derr, L. Eshed-Williams, K. Thao, S.L. Harmer and D. Zilberman, The Arabidopsis nucleosome remodeler DDM1 allows DNA methyltransferases to access H1-containing heterochromatin, *Cell* **153**, 193-205 (2016).
4. Y. Izumi, K. Fujii, F. Wien, C. Houéé-Lévin, S. Lacombe, D. Salado-Leza, E. Porcel, R. Masoud, S. Yamamoto, M, Réfrégiers, M-A. H. du Penhoat and A. Yokoya, Structure change from β-strand and turn to α-helix in histone H2A–H2B induced by DNA damage response, *Biophy. J.* **111**, 69-78 (2016).

Effects of mono-saccharides on structural stability of apo-myoglobin investigated by VUVCD spectroscopy

Takeru Shimizu[a], Munehiro Kumashiro[a], Yudai Izumi[b], and Koichi Matsuo[b]

[a]Graduate School of Science, Hiroshima University, 1-3-1 Kagamiyama, Higashi-Hiroshima, Hiroshima 739-8526, Japan
[b]Hiroshima Synchrotron Radiation Center, Hiroshima University, 2-313 Kagamiyama, Higashi-Hiroshima, Hiroshima 739-0046, Japan

Keywords: apo-myoglobin, circular dichroism, acid-denaturation, mono-saccharide, structural stability

Protein structure closely relates to the biological function. Hence the denaturation of structure due to the heat, cold, and acid (pH) induces the depression of the functions. To protect the denaturation or enhance the stability of protein structure, saccharides are often used as a stabilizer as well as polyols. Considerable efforts have disclosed that the addition of saccharides largely affects the amount of hydrations (or the numbers of water molecules) around proteins, enhancing the structural stability of proteins [1]. However, the stabilization mechanism at molecular level remains unclear. As well as proteins, saccharides are also hydrated by water molecules [2]. The numbers of water molecules depend on the structural characteristics of saccharides such as the numbers and orientations of hydroxy groups, and also it is reported that the methylation of mono-saccharides contributed to the increment of the amount of hydrations [2]. In this study, to reveal the contributions of the saccharide hydrations to the structural stability of protein, we measured the vacuum-ultraviolet circular-dichroism (VUVCD) spectra of apo-myoglobin (apoMb) at the acid-unfolded (AU) state in the presence of four types of mono-saccharides (D-Glucose (glc), methyl β-D-glucose (β-glc), D-xylose (xyl), and methyl β-D-xylose (β-xyl)).

The VUVCD spectra of apoMb were measured in the presence or absence of mono-saccharides. In the case of the absence of mono-saccharides, the helical content of apoMb at the native state (pH 6) was 76%, but that at the AU state (pH 2) decreased to only 7.7% owing to the acid denaturation (Fig. 1). Adding glc, β-glc, xyl, and β-xyl, the helical content increased to 17.8, 20.0, 10.4, and 54.5%, respectively (Fig. 1), showing that the folded structure of the native state was recovered from the acid denaturation. Considering the free energy of acid-denaturation of apoMb, it was indicated that the correlations between the amount of hydration of mono-saccharide and the structural stability of proteins would be positive.
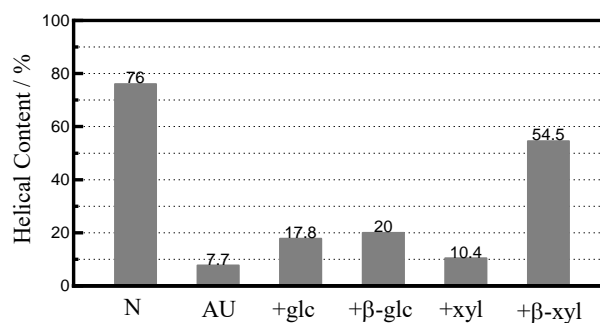
Figure 1. Helical contents of ApoMb at pH 2 (AU) in the presence of glc, β-glc, xyl, and β-xyl. The results of native (pH 6; N) and AU states are also described for comparisons.

REFERENCES

1. S. N. Timasheff, "Preferential interaction of water and cosolvents with proteins," in *Protein-Solvent Interactions*, edited by R. B. Gregory: Marcel Dekker, pp. 445-482 (1995)
2. S. A. Galema, H. Hoeiland, "Stereochemical aspects of hydration of carbohydrates in aqueous solutions. 3. Density and ultrasound measurements". *J. Phys. Chem.* **95**, 5321-5326 (1991).

Vacuum-Ultraviolet Circular Dichroism of Sucralose

Yasuyuki Maki[a] and Koichi Matsuo[b]

[a]Kyushu University, Fukuoka 819-0395

[b] Hiroshima Synchrotron Radiation Center, Hiroshima University, Higashi-Hiroshima 739-8526

Keywords: Saccharide, Artificial sweetener, Vacuum-ultraviolet circular dichroism.

Sucralose (1,6-dichloro-1,6-dideoxy-β-D-fructofuranosyl-4-chloro-4-deoxy-α-D-galactopyranoside) is one of artificial sweeteners and has emerged as one of the most commercially useful compounds in the field of sucrochemistry [1]. It is a trichlorinated derivative of sucrose synthesized by selective chlorination of sucrose at three of the primary hydroxyl groups. Its biological functions have been intensively studied but its conformations in aqueous solution are poorly understood, although they could be related to its functions.

Vacuum-ultraviolet circular dichroism (VUVCD) spectroscopy is an effective tool for analyzing saccharide structure in aqueous solution because they contain high-energy chromophores such as hydroxyl groups and acetal bonds whose electronic transitions are only detectable in the vacuum-ultraviolet (VUV) region below 190 nm [2-4]. VUVCD data accumulated for various types of saccharides still have not been fully assigned [4], but in the case of a substituted saccharide such as sucralose, comparison of the spectrum with that of the unsubstituted one may be informative for the assignment. In this study, a VUVCD spectrum of sucralose in aqueous solution was measured using a VUVCD spectrophotometer with a synchrotron radiation (SR) light source and was compared with that of sucrose.

Sucrose (FUJIFILM Wako Pure Chemical Corp.) and sucralose (Sigma-Aldrich) were used without further purification. The sample solutions were prepared by dissolving them in de-ionized water at concentrations of 10 wt%. The VUVCD spectra were measured from 262 to 172 nm at 25 $^{\circ}$C under a nitrogen atmosphere using the SR-VUVCD spectrophotometer of Hiroshima Synchrotron Radiation Center (BL-12) [5,6]. The CaF$_2$ optical cell with 50 μm path length or the SiO$_2$ optical cell with 10 μm path length was used.

Figure 1 shows the VUVCD spectrum of the aqueous sucralose solution. The CD spectrum of sucralose was observed only below 192 nm. It would have a positive peak below 180 nm, of which the position cannot be specified because of the limited wavelength range. In Figure 1, the VUVCD spectrum of the aqueous sucrose solution was also shown. The CD spectrum of sucrose was observed only below 200 nm. The peak was not observed in the present wavelength range, but there should be a positive peak below 172 nm. The molar ellipticity values of sucralose was much smaller than those of sucrose. It is not obvious if this difference is attributed to the effect of the substituent or the different molecular conformation between sucralose and sucrose, which will be the subject of the future work.
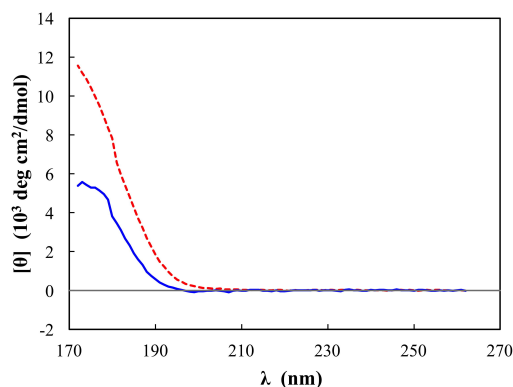
FIGURE 1. VUVCD spectra of sucralose (solid blue line) and sucrose (dotted red line) in aqueous solutions at 25 $^{\circ}$C.

REFERENCES

1. H. Zhang, S. Sun, Y. Wang and J. Cao, *Spectrochim. Acta A: Mol. Biomol. Spectrosc.* **187**, 92-97 (2017).
2. K. Matsuo, *Biomed. Spectrosc. Imaging* **6**, 111-121 (2017).
3. K. Matsuo, H. Namatame, M. Taniguchi and K. Gekko, *J. Phys. Chem. A* **116**, 9996-10003 (2012).
4. K. Matsuo and K. Gekko, *Carbohydr. Res.* **339**, 591-597 (2004).
5. K. Matsuo, K. Sakai, Y. Matsushima, T. Fukuyama and K. Gekko, *Anal. Sci.* **19**, 129-132 (2003).
6. N. Ojima, K. Sakai, K. Matsuo, T. Matsui, T. Fukazawa, H. Namatame, M. Taniguchi and K. Gekko, *Chem. Lett.* **30**, 522-523 (2001).

Secondary-Structure Analysis of DNA Gyrase Inhibitor Derived from *Staphylococcus aureus* by Vacuum-Ultraviolet Circular-Dichroism Spectroscopy

Fuminori Kato[a] and Koichi Matsuo[b]

[a]Graduate School of Biomedical and Health Sciences, Hiroshima University,
1-2-3 Kasumi, Minami-ku, Hiroshima 734-8553, Japan
[b]Hiroshima Synchrotron Radiation Center, Hiroshima University,
2-313 Kagamiyama, Higashi-Hiroshima 739-0046, Japan

Staphylococcus aureus is a Gram-positive pathogenic bacterium causing various diseases including minor skin infections to life-threatening diseases. Multidrug-resistant strains, including methicillin-resistant *S. aureus* (MRSA), make therapy against *S. aureus* infections increasingly difficult. There is an urgent need to develop new therapeutic approaches and identify novel targets for drugs against this pathogen [1].

Until now, we have found and revealed the function of novel DNA gyrase inhibitor encoding a 50-residue peptide in the *Staphylococcus aureus* genome. Bacteria have four DNA topoisomerases that are coordinated to maintain DNA topology for replication, transcription, and recombination. DNA gyrase is an essential topoisomerase and is unique to bacterial cells [2]. Therefore, DNA gyrase inhibitors cause a growth arrest and cell death in bacteria. DNA gyrase is also the target of quinolone and aminocoumarin antibiotics.

Recently, we demonstrated that amino acid substitution at the 27th Glu or the 37th Asp residues of the DNA gyrase inhibitor caused a reduction of its biological activity in *E. coli* cell (Fig. 1). However, we lack information about the protein structure and the role of these amino acid residues in its biological activity. In this study, we aimed to determine the secondary structure of DNA gyrase inhibitor by comparing ProS2-tagged DNA gyrase inhibitor with a soluble tag protein ProS2 [3], thus providing important insight into structure-function relationship for this DNA gyrase inhibitor.

Vacuum-ultraviolet circular-dichroism (VUVCD) measurements were carried out on the ProS2-tagged DNA gyrase inhibitor and ProS2-tag protein at the BL12 beamline of the Hiroshima Synchrotron Radiation Center. The secondary structure contents of ProS2-tagged DNA gyrase inhibitor and ProS2-tag protein were estimated using SELCON3 program [4]. The DNA gyrase inhibitor contained 22.9% α-helix, 6.7% β-strand, 27.5% turn, and 42.7% unordered structures (Table 1). To determine the position of the α-helical and β-strand segments, the sequence-based prediction of the secondary structure segments was performed by combining the VUVCD spectral data with the Neural Network algorithm (VUVCD-NN method) [5]. The 22nd-33rd residues and the 18th-20th residues of the DNA gyrase inhibitor formed an α-helix and a β-strand structure, respectively (Fig. 2). Interestingly, the 27th Glu residue, critical for the biological activity, was located at the center of the α-helix structure. Further, the DNA gyrase inhibitor derivatives containing E27D or D37Q amino acid substitution have folded its secondary structure correctly in comparison to the native DNA gyrase inhibitor. These results give insight into the role of the 27th Glu and the 37th Asp residues in the DNA gyrase inhibitor required for its biological activity.
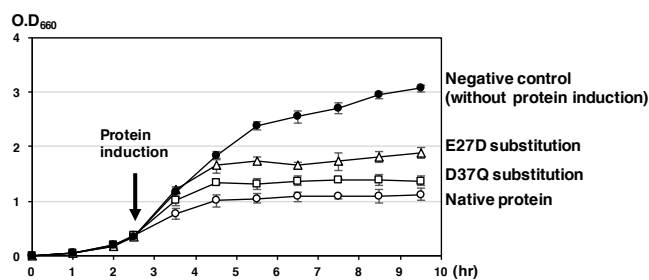
FIGURE 1. The effect of DNA gyrase inhibitor, its derivatives (E27D, and D37Q) on *E. coli* cells. *E. coli* BL21(DE3) strains were cultured in M9 GLY medium. Arabinose was added to a final concentration of 0.2% after 2.5 h (OD$_{660}$ 0.3-0.4). The arrows indicate the time point of protein induction. DNA gyrase is an essential enzyme for a bacterial cell, therefore DNA gyrase inhibitors show a reduction in bacterial cell growth.

TABLE 1. Contents of secondary structures of ProS2 tag protein and ProS2-tagged DNA gyrase inhibitor obtained using SELCON3 program.

Structure content (%)	α-helix	β-strand	Turn	Unordered
ProS2 tag	8.53	46.56	20.66	24.25
ProS2-tagged DNA gyrase inhibitor	11.45	38.50	22.06	27.99
DNA gyrase inhibitor	22.94 (%)	6.75 (%)	27.59 (%)	42.72 (%)
No. of amino acids	11.7 (A.a)	3.4 (A.a)	12.0 (A.a)	21.7 (A.a)

FIGURE 2. Sequence-based secondary structure of DNA gyrase inhibitor obtained by the VUVCD-NN method. The α-helix (H), β-strand (E), and coil (C) structures are shown by cylinder, arrow, and line, respectively. Asterisks represent the 27th Glu and the 37th Asp residues.

REFERENCES

1. Tacconelli E, Magrini N. "Global priority list of antibiotic-resistant bacteria to guide research, discovery, and development of new antibiotics." World Health Organization, Geneva, Switzerland. 2017 Feb 27.
2. Champoux JJ. "DNA topoisomerases: structure, function, and mechanism", *Annu Rev Biochem*. **70**, pp. 369-413 (2001).
3. Kobayashi H, Swapna GV, Wu KP, Afinogenova Y, Conover K, Mao B, Montelione GT, Inouye M. "Segmental isotope labeling of proteins for NMR structural study using a protein S tag for higher expression and solubility", *J Biomol NMR*, **52**, pp. 303-13 (2012).
4. Sreerama N and Woody RW, "Estimation of protein secondary structure from circular dichroism spectra: comparison of CONTIN, SELCON, and CDSSTR methods with an expanded reference set", *Anal Biochem*, **287**, pp. 252–260 (2000)
5. Matsuo K, Watanabe H, Gekko K, "Improved sequence-based prediction of protein secondary structures by combining vacuum-ultraviolet circular dichroism spectroscopy with neural network", *Proteins: Struct Funct Bioinf*. **73**, pp. 104–112 (2008).

Spectrum Measurement of Human *De Novo* Evolved Gene Product NCYM Using Vacuum-Ultraviolet Circular Dichroism

Tatsuhito Matsuo[a], Yusuke Suenaga[b], Koichi Matsuo[c], and Taro Tamada[a]

[a]*Institute for Quantum Life Science, National Institutes for Quantum and Radiological Science and Technology, Ibaraki, Japan*
[b]*Department of Molecular Carcinogenesis, Chiba Cancer Center Research Institute, Chiba, Japan*
[c]*Hiroshima Synchrotron Radiation Center, Hiroshima University, Hiroshima, Japan*

Non-genic regions in eukaryotic genomes produce noncoding RNAs, and mutations in these regions during evolution generate new lineage-specific coding genes, called de novo genes [1]. We previously found that NCYM, a cis-antisense gene of the MYCN oncogene that was believed to be a long noncoding RNA, is a human de novo gene that encodes a homininae-specific protein that promotes metastases in human neuroblastomas [2]. To understand the molecular basis underlying this function, structural characterization of NCYM is needed. NCYM is expected to show high molecular flexibility, and its character is unsuitable to determine its structure by high-resolution methods such as protein crystallography. Therefore, we employed the vacuum-ultraviolet circular dichroism (VUV-CD) to study the secondary structure of NCYM. Furthermore, we also measured the perdeuterated-NCYM to see isotopic effects on its structure.

In this beamtime, the measurements were conducted on the following samples in addition to the solvents:
(1) Hydrogenated NCYM (Tagged), 1.1 mg/ml
(2) Perdeuterated NCYM (Tagged), 1.4 mg/ml
(3) Hydrogenated Tag, 0.6 mg/ml
(4) Perdeuterated Tag, 1.4 mg/ml
The chemical composition of the solvents was 20 mM phosphate buffer (pH or pD 8.0), 3 mM DTT.

The measured VUV-CD spectra are shown in Figure 1. Significant differences in the spectra are seen in the wavelength range of 190–240 nm between the tagged proteins and the tags. These differences should arise from the spectra of NCYM.

Secondary structure contents of these samples were analyzed using these CD spectra and SELCON3 program [3, 4]. As a result, it was found that the hydrogenated tag (129 residues) contains ~14% of α-helices and ~29% of β-sheets, which are in good agreement with those calculated from the atomic structure of the tag. The tagged hydrogenated NCYM

FIGURE 1. VUV-CD spectra of H-NCYM (blue), D-NCYM (red), H-Tag (green), and D-Tag (orange). The CD spectra were measured over the wavelength range of 175–260 nm with a resolution of 1 nm.

(238 residues) was found to contain ~17% of α-helices and ~27% β-sheets, indicating that NCYM without the tag also contains secondary structures. The isotopic effects appear to be marginal, but the detailed analysis is currently underway.

REFERENCES

1. McLysaght, A. and Guerzoni, D., Phil. Trans. R. Soc. B **370**, 20140332 (2015).   2. Suenaga, Y. et al., PLoS Genetics **10**, e1003996 (2014).   3. Sreerama, N. and Woody, R.W., Anal. Biochem., **287**, 252-260 (2000).   4. Matsuo, K. et al., J. Biochem., **138**, 79-88 (2005).

Ultrafast Charge Transfer Dynamics on Partially Fluorine-Substituted Aromatic Monolayers Analyzed by Auger Electron Spectroscopy

Shin-ichi Wada[a,b], Yoshiki Iyobe[a], and Atsunari Hiraya[a,b]

[a]Department of Physical Science, Hiroshima University
[b]Hiroshima Synchrotron Radiation Center, Hiroshima University

Keywords: Self-assembled monolayers (SAMs), Resonant Auger electron spectroscopy (RAES), Core-hole-clock (CHC) method, Molecular conductivity

Charge transfer dynamics at organic interfaces has attractive potential for future applications based on organic molecular devices. We consider that such dynamics can be evaluated by resonant core-excitations. Especially, core-hole clock (CHC) method is a powerful technique to measure ultrafast charge transfer dynamics. Generally, resonant Auger decay only occur after a resonant core-excitation below ionization threshold, and normal Auger decay takes place after direct core-ionization. But normal Auger electron can be also observed in resonantly excited solid surfaces. This is caused by fast dissipation of the excited electron to conductive band of the substrate before core-hole decay. So, we can get information about such charge transfer dynamics from branching ratio between resonant Auger and normal Auger yields in comparison with the core-hole lifetime [1,2]. Actually, we have successfully measured the ultrafast charge transfer for well-ordered, self-assembled monolayers (SAMs) with aromatic molecular chains as strong reduction of resonant (spectator) Auger components in comparing with absorption intensity (total Auger yields). We have confirmed that there is the critical relationship between site-selective ion desorption and ultrafast charge transfer dynamics [3]. Such charge transfer takes place along molecular chains via molecular orbitals of excited resonant states. So, substitution of aromatic skeleton, especially fluorine-substitution which makes localization of delocalized π electrons, affects charge transfer dynamics. In this study, we studied ultrafast charge transfer dynamics on partially fluorine-substituted aromatic monolayers by measuring resonant Auger electron spectra.

Measurements of near edge X-ray absorption fine structure (NEXAFS) and Auger electron spectra were performed at the beamline BL-13 of HiSOR. During measurements, the experimental chamber had a base pressure of about 5×10^{-9} Torr. NEXAFS spectra around the O K-edge were recorded in total electron yield (TEY) mode by measuring a sample drain current. Resonant Auger electron spectra were measured using a concentric hemispherical analyzer (Omicron EA125U5) by changing photon energy of irradiation light in the O K-edge region.

Fig. 1 shows the schematic drawings of SAMs used in this study. SAMs were prepared by immersing Au substrates into 1.0 mM ethanol solutions of MFB ($HSC_6H_4C_6F_4COOCH_3$) and MBF ($HSC_6F_4C_6H_4COOCH_3$) as well as previously studied SAMs of M2P ($HSC_6H_4C_6H_4COOCH_3$) and MHDA ($HS(CH_2)_{15}COOCH_3$) [3]. All samples have $-COOCH_3$ at head groups, and MFB, MBF, and M2P have conductive phenyl rings ($-C_6H_4C_6H_4-$) at the molecular chain, while MHDA has an insulating aliphatic methylene chain.

Fig. 2 shows the typical result measured for partially fluorine-substituted MFB SAM as well as that for non-substituted M2P as a reference. Both SAMs have oxygen atoms only on their head group $-COOCH_3$, so the TEY spectra in the O K-edge show quite similar structure each other. Total Auger yields are also similar to each other
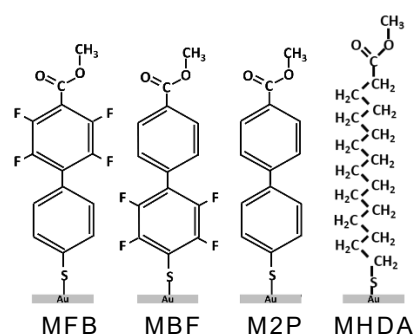
FIGURE 1. Molecular structure of SAMs used in this study, MFB, MBF, and M2P (conductive), and MHDA (insulating) SAMs.

and proportional to NEXAFS spectra. On the other hand, spectator Auger yields are strongly reduced above 533 eV. Oxygen core-electrons are resonantly excited to the unoccupied molecular orbitals around –COOCH$_3$ moieties in all SAM samples studied here. It indicates that ultrafast charge transfer from the head groups to Au substrates occurs in this energy region. The ratios of spectator Auger components of MFB (23% at 534 eV) and MBF (25%) are not so much reduced than that of M2P (18%). This result shows that the charge transfer at MFB (estimated charge transfer time 6.6 fs) and MBF (8.8 fs) is slower than M2P (3.8 fs), indicating that substitution of electron-accepting fluorine atoms cut off π conjugation of unoccupied molecular orbitals and intercept ultrafast charge transfer from their head groups to Au substrates.

REFERENCES

1. J. Schnadt, P. A. Bruhwiler, L. Patthey, J. N. O'Sea, S. Sodergren, M. Odelius, R. Ahuja, O. Karis, M. Bassler, P. Persson, H. Siegbahn, S. Lunell, and N. Martensson, *Nature* **418**, 620-623 (2002).
2. A. Fohlische, P. Feulner, F. Hennies, A. Fink, D. Menzel, D. Sanchez-Portal, P.M. Echenique, and W. Wurth, *Nature* **436**, 373-376 (2005).
3. S. Wada, M. Ogawa, S. Hosoda, R. Koga and A. Hiraya, *HiSOR Activity Report 2016*, 111-112 (2016).
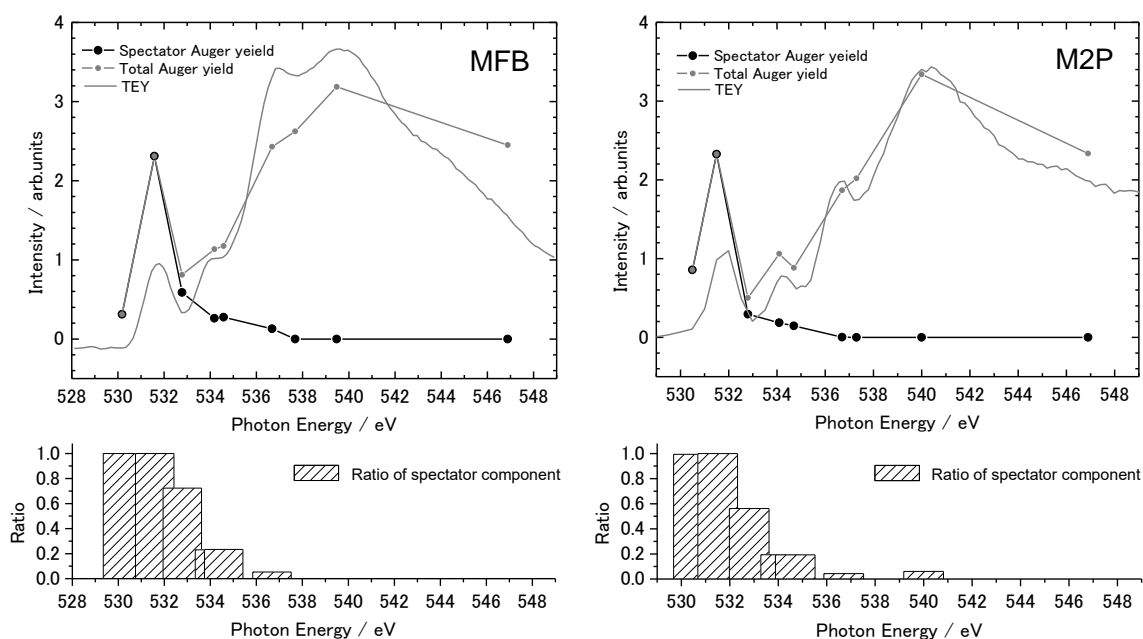
FIGURE 2. NEXAFS and Auger electron yield spectra measured for MFB (left) and M2P (right) SAMs. Gray lines show NEXAFS, and gray and black circle plots are total and spectator Auger yields, respectively. The lower bar graphs indicate the ratio of spectator components to the total Auger yields at each excitation energy.

Ion Desorption Measurements Using Pulsed HV Time-of-Flight Mass Spectrometer at HiSOR

Kamon Yamamoto[a], Atsunari Hiraya[a,b], and Shin-ichi Wada[a,b]

[a]*Department of Physical Science, Hiroshima University*
[b]*Hiroshima Synchrotron Radiation Center, Hiroshima University*

Core-excitation takes place within quite local area, so a specific atom in a molecule can be excited resonantly. Using tunable synchrotron radiation, site-selective core excitation can be achieved and site-selective bond breaking is expected in the vicinity of the atom where the primary core excitation takes place. This suggests the possibility that the resonant excitation by soft x-ray can control chemical bond scission selectively. Recently, it was found that site-selective ion desorption takes place at resonant core excitations of $C1s, O1s(OCH_3) \rightarrow \sigma^*(O\text{-}CH_3)$ and $O1s(OCH_3) \rightarrow \sigma^*(C\text{-}OCH_3)$ on surface molecules of methyl ester compounds like poly-methylmethacrylate (PMMA) thin films and self-assembled monolayers (SAMs) [1,2]. The investigation points out an importance of the primary excitation to the anti-bonding orbital localized on a specific bonding to trigger off ion desorption selectively.

Experiment using a time-of-flight mass spectrometer (TOF-MS) is a powerful approach to investigate photon stimulated ion desorption. TOF-MS combined with the pulsed synchrotron radiation from single bunch operation at KEK-PF (single bunch interval: 624 ns) has been used to measure the desorbed ion. This ion spectrometer, however, needs sufficient long SR pulse interval. In this study, to measure the desorbing ion for compact storage ring such as HiSOR (pulse interval: 73 ns), we have adapted a pulsed HV TOF-MS to the end station of BL-13 and investigated optimized measurement conditions.

BL-13 is a soft X-ray beamline in HiSOR with a Dragon-type spherical grating monochromator [3]. The beamline has been developed to investigate soft X-ray surface photochemistry and has kept a potential to measure X-ray absorption and photoelectron spectra especially for organic materials. X-ray absorption spectroscopy (XAS) as well as X-ray photoelectron spectroscopy (XPS) is a great tool to investigate element-specific electronic states of samples. So far, XAS measurements at the end station of BL-13 has been provided with the total electron yield (TEY) and total ion yield (TIY) modes. Last year, a newly built partial yield detector was installed in order to measure XAS with partial electron yield (PEY) and total fluorescence yield (TFY) modes. And this study makes partial ion yield (PIY) measurement possible in BL-13 to study spectroscopic dynamics of x-ray irradiated organic materials from various aspects.

Fig. 1 shows a schematic drawing of the pulsed HV TOF-MS adopted to the end station of BL-13. Pulsed HV was supplied to the first acceleration grid in front of sample surface to introduce desorbing ions into the drift tube and detector (from left side to right side in the figure). Typical HV was -0.5 kV and its pulse
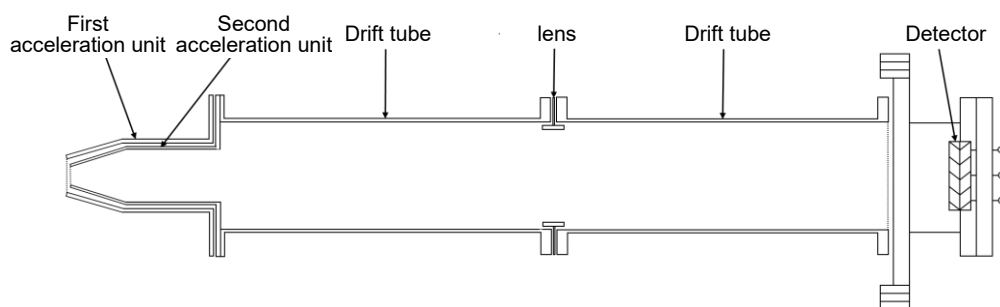
FIGURE 1. Schematic sketch of pulsed HV TOF-MS adopted to the end station of BL-13.

duration and repetition rate were several hundreds of ns and a few kHz in this study. During off-time of HV pulses, retardation voltage (typically +20 V) was also supplied to the first grid in order to store ions between the sample and first grid (Fig. 2). Although this retardation voltage helps to detect much more ion signal, we must pay attention to adjust the voltage because the voltage can also cause broadening of flight time of each ion due to various direction and magnitude of initial velocities of stored ions as shown in Fig. 2.

The other optimization of experimental setup was pulse width of HV. Typical results are summarized in Fig. 3. In supplying HV with 700 ns pulse width, we can measure CH_n^+, OCH^+, and $COCH_3^+$ ions from PMMA thin films by $C1s \rightarrow \sigma^*(O\text{-}CH_3)$ resonant core-excitation. In reducing the pulse width to 300 ns, the signal of CH_2^+ and CH_3^+ ions were well discriminated from CH_n^+ signal, while heavier ions like OCH^+ and $COCH_3^+$ were quenched. In supplying 200 ns pulse, most of ions were not detected. The result indicates the importance of suitable experimental conditions, which are still needed to adjust in order to efficiently detect desorbing ions by using pulsed HV TOF-MS.

REFERENCES

1. S. Wada, H. Kizaki, Y. Matsumoto, R. Sumii and K. Tanaka, *J. Phys.: Condens. Matter* **18**, S1629-S1653 (2006).
2. S. Wada, "Site-selective bond breaking induced by resonant core-excitations" in *Encyclopedia of Interfacial Chemistry 1st Edition - Surface Science and Electrochemistry*, edited by K. Wandelt, Amsterdam: Elsevier, 2018, pp. 621-628.
3. Homepage of Hiroshima Synchrotron Radiation Center, http://www.hsrc.hiroshima-u.ac.jp/english/storagering_beamlines/ beamlines.html.
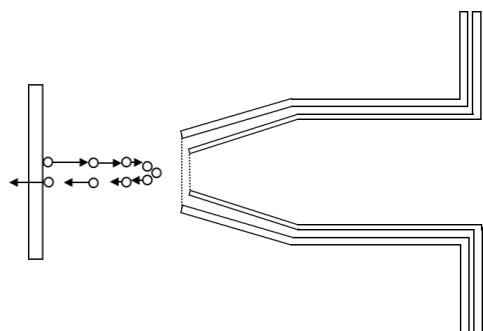
FIGURE 2. Illustration of ions stored between the sample and first grid of TOF by supplying retardation voltage. Arrows suggest velocities of each desorbing ion.
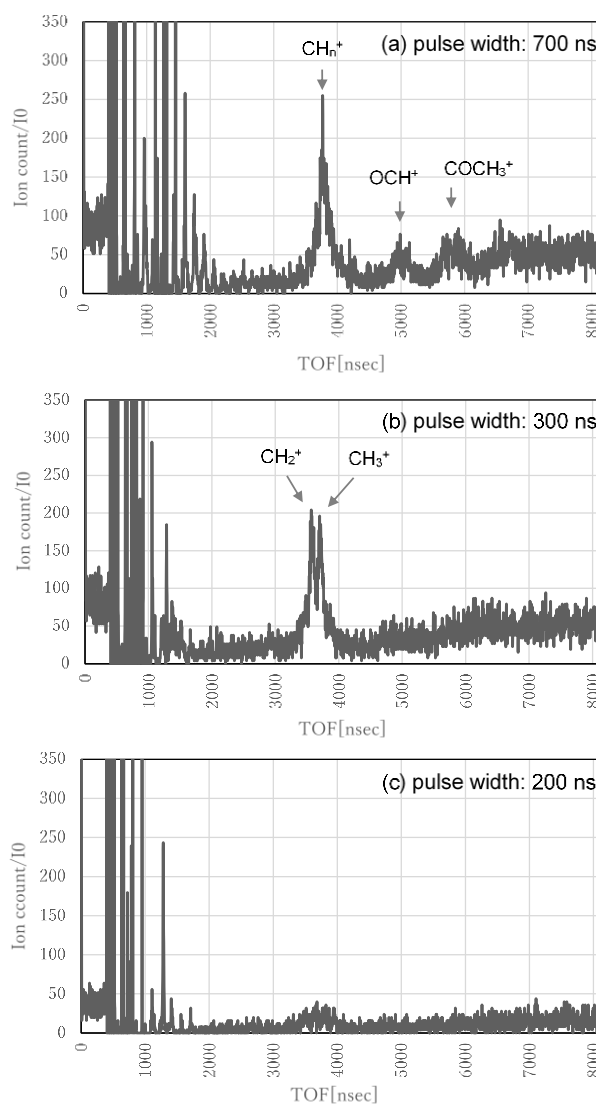
FIGURE 3. TOF spectra measured for core-excited PMMA thin films by changing pulse width of supplied HV with (a) 700 ns, (b) 300 ns, and (c) 200 ns.

Study toward Time-of-Flight Mass Spectrometry of Ion Desorption Following Inner-shell Excitation of Molecules Adsorbed on a Surface

Yasumasa Hikosaka,[a] Hiroyuki Shimada[b] and Shin-ichi Wada[c]

[a]*University of Toyama, 2630 Sugitani, Toyama, 930-0194, Japan*
[b]*KEK-IMSS-PF, 1-1 Oho, Tsukuba,305-0801, Japan*
[c]*Hiroshima University, 1-3-2 Kagamiyama, Higashi-Hiroshima, 739-8511 Japan*

Keywords: Ion desorption; Inner-shell excitation; Mass spectrometry; UMP

Ion desorption following inner-shell excitation of molecules adsorbed on a surface has attracted much attention from the viewpoint of chemical reaction control. The idea of site-selective scission of chemical bond arises from the fact that inner-shell excitation of a molecule and the subsequent Auger decay occur in the vicinity of a specific site in the molecule. One of the most conspicuous examples of the site-selective chemical bond scission induced by inner-shell excitation is observed in ester compounds adsorbed on surfaces [1]. In practice, ion desorption is not a simple result from mono-molecular reaction dynamics at Auger final states, but the energy transfer from/to surrounding molecules and the substrate also can be an important role in leading the site-selective scission.

Mass spectrometry is common tool to study ion desorption from molecules adsorbed on surfaces. Particularly, the method on the time-of-flight basis is useful for its high ion detection efficiency. The time-of-flight measurement of ions requires a pulsed light source. Wada's group has conducted time-of-flight mass spectrometry of desorbed ions using the single-bunch operation of the Photon Factory in Tsukuba [1]. The 624-ns pulse period is, however, much shorter than ion times-of-flight typically in microsecond time range, and the superimposition of peak structures resulting from different light pulses constitutes an ambiguity in spectral interpretation. Furthermore, the Photon Factory abandoned its single bunch operation several years ago, and such ion time-of-flight measurements cannot be performed now at the Photon Factory. The objective of our project which started in FY2018 is to develop a time-of-flight mass spectrometer which can operate with the continuous light from HiSOR in Hiroshima. A time-of-flight mass spectrometer in this sort was already constructed at HiSOR long ago [2], and the main components are utilized in the current project. We have carried out in FY2018 the maintenance and the preparation of a pulsed power supply and electronics circuits for applying pulsed electric field to the spectrometer electrodes. Ion time-of-flight measurements will be ready soon in the early stage of next fiscal year.

One of the target samples in our mass spectrometric study is uridine 5′-monophosphate (UMP) adsorbed on a surface. Understanding of the ion desorption following inner-shell excitation of such kind of nucleotides is important in its close connection with DNA lesions induced by ionizing radiation. A single UMP molecule contains two nitrogen atoms which locate at different chemical environments in the molecule. It is known that in the aqueous solution the chemical shift of the nitrogen 1s binding energies shows dependence on pH, due to the deprotonation of N3 atom in UMP at high pH [3]. One of our concerns is whether the deprotonation links to ion desorption following inner-shell excitation. A sample deposited on a metal or Si surface, instead of aqueous solution, is adequate to the investigation with our time-of-flight mass spectrometer. We attempted a simple method for preparing UMP sample deposited on a metal: a drop of UMP aqueous solution (~0.01 mM) of pH 11 was dried on the Au substrate during several hours. This sample preparation has a risk of contamination by manipulation in the atmosphere. To examine if the deprotonation of N3 atom keeps in the condensed UMP sample prepared by this simple method, we have measured the XANES and XPS spectra in the N-K edge range, prior to a mass-spectrometric investigation to the ion desorption. Figure 1 shows N1s photoelectron spectra measured at two different photon energies. The N 1s photoelectron structure in the spectrum measured at a photon energy of 472 eV exhibits a shoulder at the high kinetic energy side. The energy difference between the peak top and the

shoulder is about 3 eV, which is reasonable as the energy splitting for the chemical shift of the nitrogen 1s binding energies [3]. However, the observed intensity ratio of the splitting components is around 2:1, much different from the expected 1:1 peak ratio. Similar intensity ratio is observed in the photoelectron structure measured at a photon energy of 522 eV, indicating that the intensity ratio does not result from resonance effect at a particular photon energy range. While the observed peak ratio suggests a deformation of the molecular structure and the deprotonation of UMP located at the outermost surface of the condensed sample, the peak splitting implies that the deprotonation of the UMP sample keeps in the condensed sample prepared by the present method. We plans to perform mass spectrometry using this sample preparation, to give insight into ion desorption following inner-shell excitation of the condensed UMP molecules.
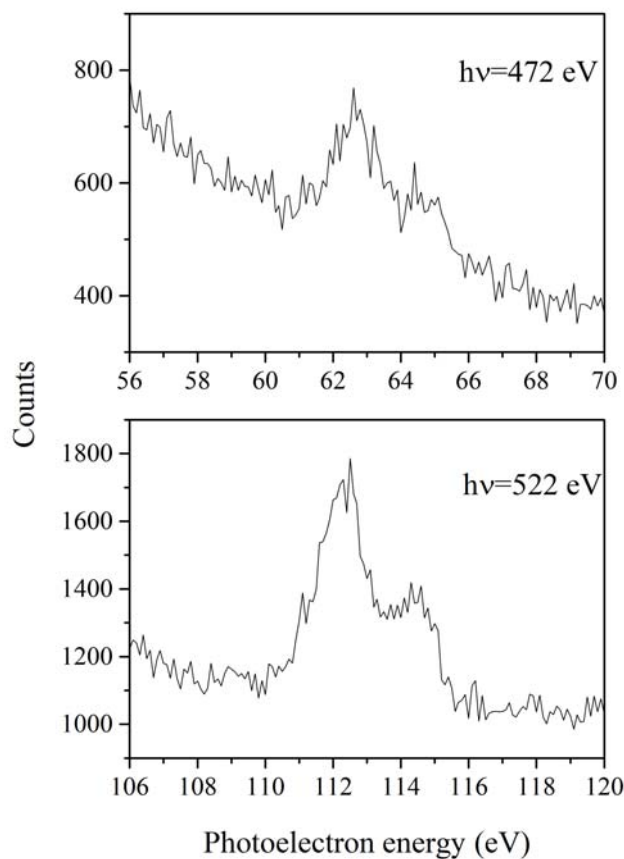
FIGURE 1. N1s photoelectron spectra measured at two different photon energies for uridine 5′-monophosphate adsorbed on an Au surface.

REFERENCES

1. S. Wada, H. Kizaki, Y. Matsumoto, R. Sumii and K. Tanaka, *J. Phys: Cond. Matt.*, 18, S1629-S1653 (2006).
2. K. Fujii, D. Taga, Y. Nakashima, S. Waki, S. A. Sardar, Y. Yasui, S. Wada, T. Sekitani and K. Tanaka, *Nucl. Instrum Meth. Phys. Res A* **467-468**, 1509-1513 (2001).
3. H. Shimada, H. Minami, N. Okuizumi, I. Sakuma, M. Ukai, K. Fujii, A. Yokoya, Y. Fukuda and Y. Saitoh, *J. Chem. Phys.* **142**, 175102 (2015).

Soft X-ray Spectroscopies for Br-incorporated DNA Nucleotide

Misaki Hirato[a,b] and Kentaro Fujii[b], Akinari Yokoya[b,c], Shin-ichi Wada[d], Yuji Baba[e]

[a]*Ibaraki University, Mito, Japan*
[b]*Tokai Quantum Beam Science Center, QST, Tokai, Japan*
[c]*Graduate School of Science and Engineering, Ibaraki University, Mito, Japan*
[d]*Graduate School of Science, Hiroshima University, Higashihiroshima, Japan*
[e] *Fukushima research and development department, JAEA, Fukushima, Japan*

Keywords: bromouracil, BrdUMP, TMP, DNA damage, XPS, XANES

The aim of the present study is to clarify the electronic states of DNA related molecules incorporating a bromine atom. Since cells with DNA incorporating 5-bromouracil (BrU) as a thymine analogue have been known to be highly sensitive to ionizing irradiation, BrU is expected to be pharmacological agents as sensitizers in radiation therapy. Previously, a radiation-track simulation study proposed a mechanism that hydrated electrons produced by water radiolysis could react with DNA incorporating bromine atoms (hereafter denoted as Br-DNA) to form damage [1]. A recent EPR study reported that the bromine atom changes the yield of unpaired electrons in the uracil moiety [2].

In order to understand the physicochemical nature of Br-DNA, we investigated the binding energies of inner shell electrons of particular atoms in the DNA molecule using X-ray photoelectron spectroscopy (XPS) and X-ray Absorption Near Edge Structure (XANES) around the energies of C, N, O and Br K-absorption edges. Thin film samples of BrU, 5-bromo-2'-deoxyuridine-5'-monophosphate (BrdUMP) and thymidine-5'-monophosphate (TMP) were used for the spectroscopies at the Photon Factory BL-27 and HiSOR BL-13.

Obtained results indicate that the photoelectron binding energies, as well as the absorption edge energies, were similar for those sample molecules regardless of binding of a bromine atom to them. Contrary to the initial expectation, it is concluded that a bromine atom does not significantly contribute to the inner shell or unoccupied states in these molecules. Effect of bromine atom on the valence electronic states should be addressed in future studies.

[1] Watanabe and Nikjoo *Int. J. Radiat. Biol.* **78**, 953-66 (2002).
[2] Oka et al. *Appl. Phys. Lett.* **113**, 243701 (2018).

X-ray absorption spectroscopy of YbCu$_x$ at Cu-L_3 absorption edge

Hitoshi Yamaoka[a] Naohitio Tsujii[b], Masahiro Sawada[c], and Kenya Shimada[c]

[a]*RIKEN SPring-8 Center, 1-1-1 Kouto, Sayo, Hyogo 679-5148, Japan*
[b]*International Center for Materials Nanoarchitectonics (MANA), National Institute for Materials Science, 1-2-1 Sengen, Tsukuba, Ibaraki 305-0047, Japan*
[c]*Hiroshima Synchrotron Radiation Center, Hiroshima University, Higashi-Hiroshima, Hiroshima 739-0046, Japan*

Recently, some Yb compounds were found to show anomalous decrease of the Yb valence at low pressures. In YbCu$_{4.5}$ a first-order valence transition to the divalent Yb state was found around 0.6-2.7 GPa [1]. This valence transition is accompanied by the structural transition at the same pressure range. In the cubic YbCu$_5$-based compounds the Yb valence was found to decrease with increasing pressure without structural phase transition at low pressures less than 10 GPa. It indicates a pressure-induced crossover from a localized $4f^{13}$ state to the valence fluctuation regime, which was not expected for Yb systems with the conventional c-f hybridization [2]. High-pressure study for the Yb-Cu binary alloy systems, YbCu, YbCu$_2$, YbCu$_{4.5}$, YbCu$_5$, and YbCu$_{6.5}$ has been performed at SPring-8. Here, complementary to the high-pressure experiments for the Yb site, we study the electronic structures for the Cu sites of the Yb-Cu binary alloy systems by x-ray absorption spectroscopy (XAS) at ambient pressure.

Figure 1(a) show high-resolution XAS spectra at the Cu-L_3 absorption edge for YbCu, YbCu$_2$, YbCu$_{4.5}$, and YbCu$_{6.5}$, being comapred with XAS spectra for YbInCu$_4$ and Cu$_2$O. Spectra for YbCu and YbCu$_2$ are similar each other. The spectrum of Cu$_2$O is in agreemwnt with the previous results [3]. The single peak around 933 eV in Cu$_2$O was assigned to a $2p^53d^{10}$ final state coming from a $2p^63d^9$ initial state [4]. The spectra of YbCu$_x$ are very different from that of Cu$_2$O, where Cu atoms are covalently bonded to the O atoms [2,5,6], and are similar to that of Cu metal [3] except YbCu$_{6.5}$. This suggests the metallic bond of the YbCu$_x$ systems. Theoretical calculations for fcc and bcc Cu metal suggested that the peak P2 at 935 eV and the peak P3 at 939 eV correspond to the transitions of $2p$-$3d$ and $2p$-$3s$, respectively [5]. From the analogy to the XAS spectra of the Cu$_2$FeS$_4$ compounds, the peaks P1, P2, and P3 could be assigned to the final states $cd^{10}Ls^2$, $cd^{10}s$, and cd^9s^2, respectively, where L denotes the ligand hole [7]. The energy of the absorption edge shifts to higher energy in the following order: YbCu < YbCu$_2$ < YbCu$_{4.5}$.

In YbInCu$_4$ a slight shift of the peak P2 to higher energy was observed with increasing the intensity of the peak P1 below the temperature of the valence transition, where the weak shoulder peak P1 was considered to be derived from the Cu $3d$ states [8]. It was suggested that across the valence transition the electron transfer from the Cu $3d$ sites to the Yb $4f$ sites occurred at low temperature, resulting in the increase of the DOS of the Yb^{2+} states near the Fermi level. The peak intensity of YbCu and YbCu$_2$ corresponding the peak P1 of YbInCu$_4$ is relatively stronger than that of YbCu$_{4.5}$. This suggests that the empty states of Cu $4d$ of the former compounds are larger than those of the latter. This explains the Yb valence of YbCu and YbCu$_2$ are smaller than that of YbCu$_{4.5}$.

The electronic structure of YbCu$_{6.5}$ is very different from others and rather similar to that of K$_2$NaCuF$_6$ [9]. YbCu$_{6.5}$ has a sharp and strong peak at 931 eV, which is not observed in YbCu, YbCu$_2$, and YbCu$_{4.5}$. Two peaks around 931 eV and 934 eV could be assigned to be Cu^{2+} and Cu^{3+} states and described as the electronic configurations of $2p^53d^{10}$ and a mixing of $3d^8$ and $3d^9L$, respectively [9]. A weak shoulder peak on the right of the 934 eV peak in YbCu$_{6.5}$ is due to the multiplet effect [9]. In K$_2$NaCuF$_6$ the charge transfer energy (Δ) was considered to be negative, where Δ is equivalent to the energy difference between $3d^8$ and $3d^9L$ for the ground state [9], suggesting the negative charge transfer also in YbCu$_{6.5}$. In this case, the $3d^9L$ states are more preferred than the $3d^8$ states because the energy level of the former is lower than the latter.

Figure 1(b) shows the temperature dependence of the XAS spectra of YbCu$_{4.5}$ below 80 K. No temperature dependence was observed. In YbCu$_{4.5}$ the Yb valence decreased with decreasing the temperature from 2.94 at 100 K to 2.92 at 16 K [1]. The result in Figure 1(b) indicates that the temperature-induced change in the electronic structure of the Cu sites is too small to observe in the present resolution.

The electronic structure of the Cu sites of YbCu$_{6.5}$ is different from that of YbCu$_{4.5}$. While the Yb valence drastically decreased with pressure at low pressures in both compounds in the similar way. YbCu$_{4.5}$ is known to have a complex crystal structure and has more than two Yb sites. Present XAS spectra in Fig. 1(a) suggest that YbCu$_{6.5}$ has two kinds of Yb sites. The role of the each Yb sites in YbCu$_{4.5}$ and YbCu$_{6.5}$ under pressure is unknown and remains as an interesting study in the future because both compounds show the pressure-induced anomaly and have the multi-Yb sites in common.
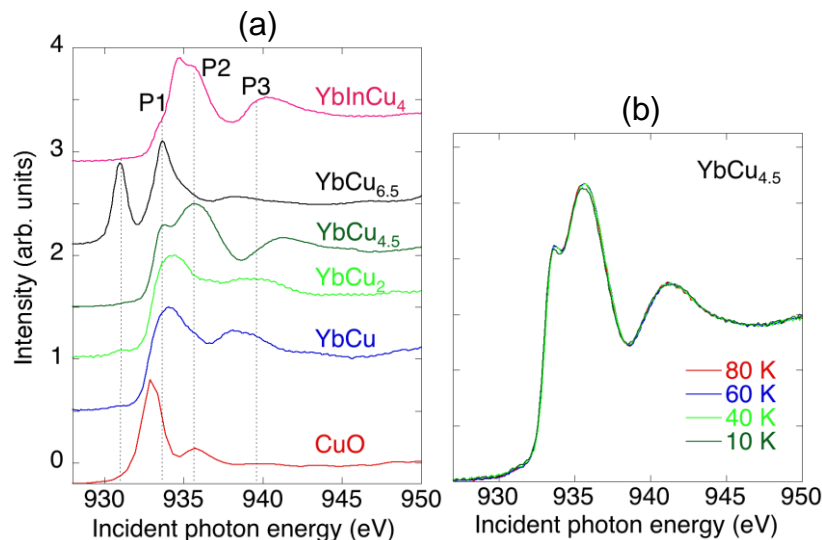
FIGURE 1. (a) XAS spectra of YbCu, YbCu$_2$, YbCu$_{4.5}$, YbCu$_{6.5}$, and YbInCu$_4$ at 10 K with that of Cu$_2$O at 300 K. (b) Temperature dependence of the XAS spectra of YbCu$_{4.5}$.

REFERENCES

1. H. Yamaoka, N. Tsujii, Y. Yamamoto, Y. Michiue, J.- F. Lin, N. Hiraoka, H. Ishii, K.-D. Tsuei, and J. Mizuki, Reentrant valence transition in YbCu$_{4.5}$ under pressure, *Phys. Rev. B* **97**, 085106 (2018).

2. H. Yamaoka, N. Tsujii, M.-T. Suzuki, Y. Yamamoto, I. Jarrige, H. Sato, J.-F. Lin, T. Mito, J. Mizuki, H. Saku- rai, O. Sakai, N. Hiraoka, H. Ishii, K.-D. Tsuei, M. Gio- vannini, and E. Bauer, Pressure-induced anomalous valence crossover in cubic YbCu$_5$-based compounds, *Sci. Rep*. **7**, 5846 (2017).

3. M. Finazzi, G. Ghiringhelli, O. Tjernberg, Ph. Ohresser, and N. B. Brookes, Radiationless Raman versus Auger behavior at the Cu L_3 resonance of CuO and Cu$_2$O, *Phys. Rev. B* **61**, 4629 (2000).

4. M.-J. Huang, G. Deng, Y. Y. Chin, Z. Hu, J.-G. Cheng, F. C. Chou, K. Conder, J.-S. Zhou, T.-W. Pi, J. B. Good- enough, H.-J. Lin, and C. T. Chen, Determination of hole distribution in Sr$_{14-x}$Ca$_x$Cu$_{24}$O$_{41}$ using soft x-ray absorption spectroscopy at the Cu *L*3 edge, *Phys. Rev. B* **88**, 014520 (2013).

5. H. Ebert, J.Stöhr,S. S. P. Parkin, M. Samant, and A. Nilsson, *L*-edge x-ray absorption in fcc and bcc Cu metal: Comparison of experimental and first-principles theoretical results, *Phys. Rev. B* **53**, 16067 (1996).

6. P. Jiang, D. Prendergast, F. Borondics, S. Porsgaard, L. Giovanetti, E. Pach, J. Newberg, H. Bluhm, F. Besenbacher, and M. Salmeron, Experimental and theoretical investigation of the electronic structure of Cu$_2$O and CuO thin films on Cu(110) using x-ray photoelectron and absorption spectroscopy, *J. Chem. Phys*. **138**, 024704 (2013).

7. R. A. D. Pattrick, G. Van Der Laan, J. M. Charnock, and B. A. Grguric, Cu L_3 x-ray absorption spectroscopy and the electronic structure of minerals: Spectral variations in non-stoichiometric bornites, Cu$_5$FeS$_4$, *American Mineralogist* **89**, 451 (2004).

8. Y. Utsumi, H. Sato, H. Kurihara, H. Maso, K. Hiraoka, K. Kojima, K. Tobimatsu, T. Ohkochi, S.-I. Fujimori, Y. Takeda, Y. Saitoh, K. Mimura, S. Ueda, Y. Yamashita, H. Yoshikawa, K. Kobayashi, T. Oguchi, K. Shimada, H. Namatame, and M. Taniguchi, Conduction-band electronic states of YbInCu$_4$ studied by photoemission and soft x-ray absorption spectroscopies, *Phys. Rev. B* **84**, 115143 (2011).

9. C. De Nadaï. Demourgues, and J. Grannec, $L_{2,3}$ x-ray absorption spectroscopy and multiplet calculations for K*M*F$_3$ and K$_2$Na*M*F$_6$ (*M* = Ni, Cu), *Phys. Rev. B* **63**, 125123 (2001).

Development of a Soft X Ray Reflectometer in a Low Vacuum environment at HiSOR-BL14

Tatsuya Mayumi[a], Yuka Ohashi[b], Norikazu Ichikawa[b], Masahiro Sawada[c]

[a]Department of Physical Sciences, Faculty of Science, Hiroshima University
[b]Department of Physical Science, Graduate School of Science, Hiroshima University
[c]Hiroshima Synchrotron Radiation Center, Hiroshima University

Keywords: apparatus development, soft X-ray, reflectometry

Soft X-ray reflectometry is one of useful methods for investigation of a valence electron structure, which is probed through a resonant scattering process in the vicinity of an absorption edge. Since a magneto-optical effect appears in a reflectance profile of polarized SR light, the reflectometry method can also be utilized to analysis of a magnetic state and a magnetic structure for many kind of magnetic materials including insulators. Insensitivity to sample surface of the photon-in-photon-out technique is an advantage to investigate practical materials like an electronic/spintronic device, whose region of interest are deep inside of the layered structures. Measurements under low vacuum or atmospheric pressure in helium-pass expands the capability of soft X-ray reflectometry into ambient/operando spectroscopy, whose vacuum environment can be easily established by vacuum separation technique with X-ray transmission membrane.

In this development project, we have constructed an experimental system of X-ray reflectometer connected to HiSOR-BL14, in order to realize soft X-ray reflectometry in a low vacuum environment. A device unit of reflectometer was assembled as stand-alone instrument, which was finally installed into a low vacuum chamber. The reflectometer unit consists of two motorized rotation stages for $\theta/2\theta$ scanning which are so fixed on an aluminum main flame that the rotation axes are coaxially aligned. A sample stage and a X-ray detector component are mounted on the θ and 2θ rotation stage with support arms, respectively. In the sample stage component, two-axes adjustment mechanism is installed so that a sample surface and a scattering plane can coincide with the rotation center and the $\theta/2\theta$ scanning plane, respectively. Figure 1 shows schematic views of the reflectometer unit. Mechanical alignment and evaluation of geometric tolerance were carried out using laser and a transit telescope. After our confirmation for the reflectometer to achieve good tolerance in $\theta/2\theta$ scanning, the whole instrument was completely build up including electrical and vacuum system, and it was successfully installed to a SR beamline of BL14. Practical adjustments and a first test measurement were carried out for a gold foil sample using synchrotron radiation. Figure 1 shows
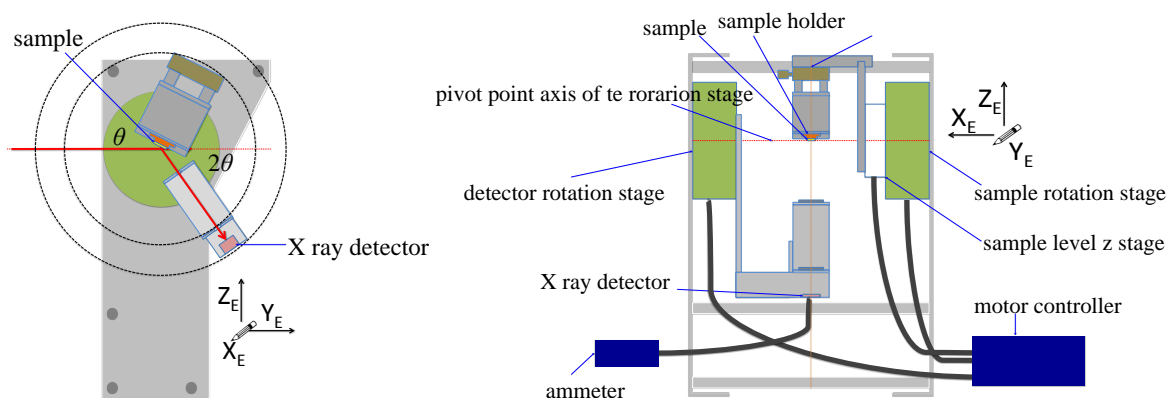
FIGURE 1. schematic view of the measurement unit

schematic views of the reflectometer unit. Mechanical alignment and evaluation of geometric tolerance were carried out using laser and a transit telescope. After our confirmation for the reflectometer to achieve good tolerance in $\theta/2\theta$ scanning, the whole instrument was completely build up including electrical and vacuum system, and it was successfully installed to a SR beamline of BL14. Practical adjustments and a first test measurement were carried out for a gold foil sample using synchrotron radiation.

REFERENCES

1. K. Sakurai, Introduction to X-ray Reflectivity,2009.
2. K. Ishii, M. Sawada, Development of a soft X-ray reflectometer in an ambient pressure or a low vacuum environment at HiSOR-BL14, 2018. (Japanese)

Magnetic properties of Co ultrathin films intercalated underneath monolayer h-BN grown on Ni(111) probed by soft X-ray magnetic circular dichroism

Yuka Ohashi[a], Norikazu Ichikawa[a], Tatsuya Mayumi[b], Masahiro Sawada[c]

[a]*Department of Physical Sciences, Graduate School of Science, Hiroshima University*
[b]*Department of Physical Sciences, Faculty of Science, Hiroshima University*
[c]*Hiroshima Synchrotron Radiation Center, Hiroshima University*

Keywords: cobalt, h-BN, nickel ; soft X-ray magnetic circular dichroism

A magnetic tunnel junction (MTJ) is a trilayer structure that consists of two ferromagnetic metallic layers and a nonmagnetic insulating layer sandwiched with them. Tunnel magnetic resistance (TMR) effect is observed in the MTJ structures, whose electrical conductivity is well known to depend on relative direction of magnetization between the two ferromagnetic layers. TMR effect is widely applied to magnetic devices such as a magnetic random access memory and a magnetic head in hard disk drive [1]. MR ratio is one of important performance indices of the TMR devices, and it is crucially affected by atomic arrangement at an interface between the ferromagnetic layer and the insulating barrier layer. Recently, MTJ structures with an insulating monolayer of hexagonal boron nitride (h-BN) is paid attention to [2], because it provides ideal flat interfaces without pinholes to be expected for improvement of the MR ratio. Since spin polarization at the interface is also important for the MR ratio, investigation of interface magnetism is essentially required for the ferromagnetic layers contacts to the h-BN monolayer.

In this research, we fabricated h-BN/Co ideal interfaces by intercalation of 0.5-7.2 ML Co ultrathin films underneath a h-BN monolayer grown on Ni (111) under ultra-high vacuum condition at HiSOR BL-14. The magnetic properties of Co ultrathin films were probed by soft X-ray magnetic circular dichroism.

Intensities of XMCD spectra at Co $L_{2,3}$ edges were observed as a function of the Co thickness. At 1 ML, antiferromagnetic spin alignment was observed, whose spin direction is opposite to the external magnetic field and magnetization of Ni substrate. This spin alignment was changed gradually into ferromagnetic spin alignment as the Co thickness was increased. The corresponding spin magnetic moment was ferromagnetically saturated near 5 ML and the estimated value was larger than bulk Co [3].

The antiferromagnetic spin alignment at 1 ML Co was disappeared by momentary exposure of oxygen on the top of h-BN monolayer. However, neither residual atoms of oxygen nor Co oxide in the ultrathin films was observed after the oxygen exposure. From this result, we can indicate the possibility that atomic structure and magnetic properties of Co ultrathin films are changed by oxygen collision on the monolayer h-BN surface.

REFERENCES

1. R. Jansen, Appl. Phys. **36**, R289 (2003).
2. M. Piquemal-Banci, et al. Appl. Phys. Lett., **108**, 102404 (2016).
3. C. T. Chen, et al. Phys. Rev. Lett., **75**, 152 (1995).

Antiferromagnetic coupling at the interface of Co/h-BN/Ni(111) studied by soft X-ray magnetic circular dichroism

Norikazu Ichikawa[a], Yuka Ohashi[a], Tatsuya Mayumi[b],
Masahiro Sawada[c], Akio Kimura[a]

[a]*Department of Physical Sciences, Graduate School of Science, Hiroshima University,*
1-3-1 Kagamiyama, Higashi-Hiroshima, 739-8526, Japan
[b]*Department of Physical Sciences, Faculty of Science, Hiroshima University,*
1-3-1 Kagamiyama, Higashi-Hiroshima, 739-8526, Japan
[c]*Hiroshima Synchrotron Radiation Center, Hiroshima University,*
2-313 Kagamiyama, Higashi-Hiroshima, 739-0046, Japan

Tunnel magnetoresistance (TMR) effect is one of key phenomena for developing of spintronic devices. Monolayer hexagonal boron nitride is an insulating layered material with stable honeycomb structure. It is expected to provide an ideal barrier layer in magnetic tunnel junction (MTJ), where a pinhole-less ultrathin barrier layer ensures large MR ratio and low power consumption. Spin-dependent transport studies with the MTJ incorporating a monolayer h-BN have shown the MR ratio up to 150% at room temperature [1, 2]. So far, magnetic state at the interface between a magnetic layer and a monolayer h-BN has not been sufficiently clarified, although it takes an essential role in a mechanism of TMR. To clarify magnetic state at the interface between a magnetic layer and monolayer h-BN, we have investigated magnetic properties of Co layers in Co/h-BN/Ni(111) structure by means of soft X-ray magnetic circular dichroism (XMCD) spectroscopy.

We fabricated Co wedge films on h-BN/Ni(111) films for this purpose. High-quality h-BN monolayer was prepared on a Ni(111) surface by cracking of vaporized borazine ($B_3N_3H_6$) [3]. The samples of Co/h-BN/Ni(111) are obtained by MBE evaporation of Co at room temperature. The XMCD experiments were *in-situ* performed at HiSOR-BL14 [4, 5]. Figure 1 shows the XMCD spectrum measured at room temperature at Co and Ni $L_{2,3}$ edges in normal incidence geometry under the external magnetic field of 1.1 T along sample normal direction. The Co magnetic moment is antiferromagnetically saturated below 2.3 ML whose direction
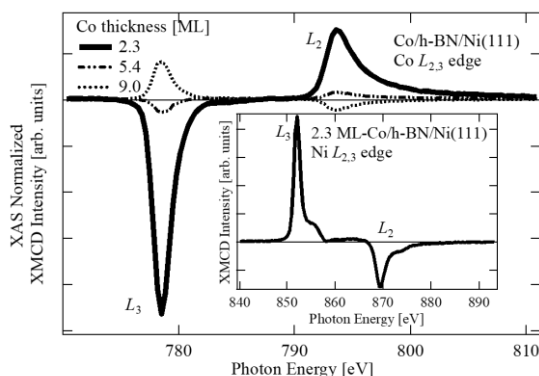
FIGURE 1. XMCD spectrum at Co $L_{2,3}$ edge and Ni $L_{2,3}$ edge in normal incidence geometry with magnetic field of 1.1 T along sample normal direction

is opposite to Ni spin and external magnetic field. As the Co film thickness is increased, the antiferromagnetic coupling (AFC) is gradually released by increasing energy gain of ferromagnetic alignment parallel to the field. This indicates that only a Co monolayer at the interface is antiferromagnetically coupled. We estimated a quantitative value of AFC energy between Ni and a Co monolayer at the interface by analyzing Co thickness dependence of *M-H* curves derived from field dependent XMCD signals. As a result, we have found the AFC energy is about 25 meV/atom. A previous study has suggested hybridization between h-BN π and Ni 3d orbitals leading to spin polarized gap states at the nitrogen site [6]. Considering charge transfer effect from the spin polarized π-orbital of nitrogen to d_{z^2}-orbitals of cobalt, we calculated the AFC energy based on second-order perturbation in an electron hopping process between their orbitals. From good agreement between the estimated AFC energy and the experimental value, we have concluded the AFC between Co and Ni at the interface results from superexchange interaction via h-BN.

REFERENCES

1. A. Dankert, M. V. Kamalakar, A. Wajid, R. S. Patel, and S. P. Dash, Nano. Res. **8**, 1357 (2015).
2. M. Piquemal-Banci, R. Galceran, S. Caneva, M. -B. Martin, R. S. Weatherup, P. R. Kidambi, K. Bouzehouane, S. Xavier, A. Anane, F. Petroff, A. Fert, J. Robertson, S. Hofmann, B. Dlubak, and P. Seneor, Appl. Phys. Lett. **108**, 102404 (2016).
3. C. Oshima and A. Nagashima, J. Phys.: Condens. Matter **9**, 1 (1997).
4. M. Sawada, K. Yaji, M. Nagira, A. Kimura, H. Namatame, M. Taniguchi, AIP Conf. Proc. **879**, 551 (2007).
5. M. Sawada, T. Ueno, T. Tagashira, H. Namatame, M. Taniguchi, AIP Conf. Proc. **1234**, 939 (2010).
6. A. B. Preobrajenski, S. A. Krasnikov, A. S. Vinogradov, May Ling Ng, T. Käämbre, A. A. Cafolla, and N. Mårtensson, Phys. Rev. B **77**, 085421 (2008).

Cation Distribution and Magnetic Properties of NiFe$_2$O$_4$ Nanofilms on MgO and SrTiO$_3$ substrates: XAS and XMCD Soft X-ray Studies

Andrey K. Kaveev,[a] Alexander G.Banshchikov[a], Nikolay S. Sokolov[a] and Masahiro Sawada[b]

[a]Ioffe Institute, 194021, 26 Polytechnicheskaya str., Saint-Petersburg, Russia
[b]Hiroshima University, 739-8527, Higashi Hiroshima, Japan

Keywords: Spinel ferrite, NiFe$_2$O$_4$, cation distribution.

Among spinel-type materials nickel ferrite (NiFe$_2$O$_4$, NFO) represents a known insulating material. It is attractive properties demanded in RF and microwave applications are a reason of intensive studies of this material since the middle of 20th century. The necessity of modern spintronic and magnonic devices require NFO films with thickness in the nanometer range. However, such films usually exhibit magnetic properties that are inferior to those of the bulk crystals. Studies of ultrathin (2-10 nm) films attractive for spin filtering have been carried out in Ref. [1]. Lately excellent magnon transport properties of 40 and 450 nm thick NFO films on MgGa$_2$O$_4$ substrates has been demonstrated in Ref. [2]. In this work, 10-250 nm thick NFO films were grown on SrTiO$_3$ (STO) and MgO(001) substrates by laser molecular beam epitaxy in a wide range of growth conditions. XMCD spectra of the films were studied depending on the growth parameters.
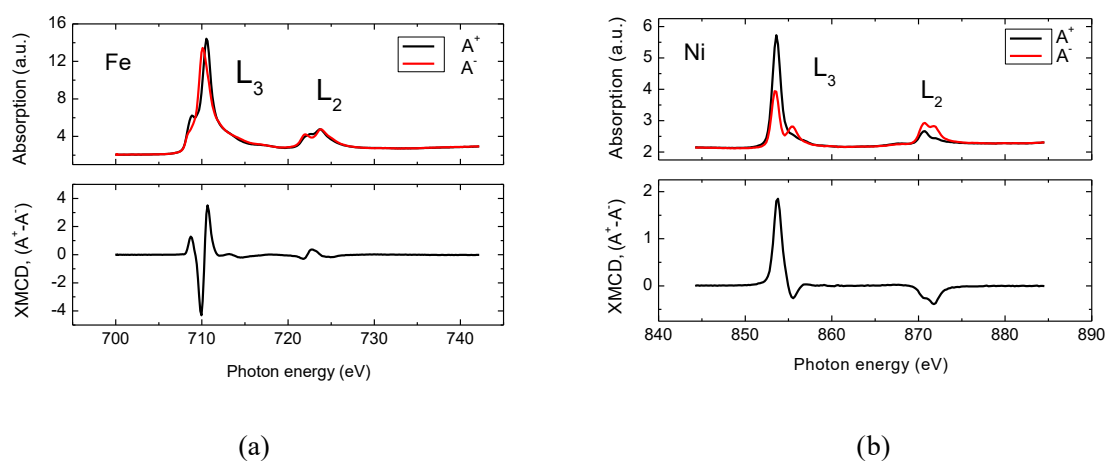
FIGURE 1. Characteristic XAS and XMCD spectra for L$_{2,3}$ edges of Fe (a) and Ni (b) for the NFO/STO(001) film grown at 1000°C with the subsequent annealing in the air.

Thin NFO films (1-100 nm) were grown with the use of laser molecular beam Epitaxy on MgO and SrTiO3 substrates at the different growth conditions. XRD and RHEED measurements showed high crystal quality of the films.

It was found that NFO films grown on STO(001) at elevated temperatures (1000°C) with post-growth annealing at 1100°C have strong XMCD signal as for Fe, so for Ni (see Fig. 1). In the first case large signal is related to main absorption L$_3$ peak shift at 0.6 eV after an applied field direction inversion. In the

second case large XMCD signal exceeds that observed in Refs. [3-5]. According to Ref. [6], magnetic moments of metals in octahedral (O_h) and tetrahedral (T_d) environments in spinels are antiparallel. The largest of these moments is oriented parallel to the applied external magnetic field direction. The magnetic moment of atoms situated in O_h environment is higher, because of twice larger amount of octahedral sites than amount of tetrahedral sites (in the case of inverted spinel the moment is defined by two types of atoms, in contrast to the case of normal spinel with only one type of atoms), and taking into account characteristic values of the moments: 5 μB for Fe^{3+}, 4 μB for Co^{3+}, 2.3 μB for Ni^{2+}. This means that the magnetic moment in the O_h environment is oriented parallel to the external magnetic field direction, the magnetic moment in the T_d environment is oriented antiparallel. Moreover, the XRD signal sign at the L_3 absorption edge, and, hence, the sign of the Ni magnetic moment, corresponds to that of clear metallic Ni measured at the same conditions (not shown there). Therefore, all Ni magnetic moments in NFO films measured in the experiment, are collinear to the external magnetic field direction. This means that the NFO spinel in our case is completely inverted, i.e. there are no Ni atoms in the T_d environment. It is in agreement with the simulation results. This circumstance distinguishes our results from the obtained in Refs. [3-6], where the value of the Ni magnetic moment is smaller. The samples prepared in this way are the most promising from the point of view of the spin wave propagation in the NFO films. In case the NFO growth on MgO(001) the situation is not so straightforward, because of possible intermixed the materials at the interface during the growth and annealing at elevated temperatures.

REFERENCES

1. V.G.Harris et al., *J.Magn.Magn.Mater.***321,** 2035–2047 (2009).
2. J.Shan et al., *Appl.Phys.Lett*., **113,** 162403 (2018).
3. M.C. Richter, J.-M. Mariot, et al, *Eur. Phys. J. Spec. Topics,***169**, 175–180 (2009).
4. V. K. Verma,V. R. Singh et al., *Phys. Rev. B*, **89**, 115128 (2014).
5. C. Klewe, M. Meinert at al., *J. Appl. Phys*., **115**, 123903 (2014).
6. L. Néel, *Ann. Physique*, **3**, 137, (1948).

Investigation of multi-mode spin–phonon coupling and local B-site disorder in Pr_2CoFeO_6 by Raman spectroscopy and correlation with its electronic structure by XPS and XAS studies

Arkadeb Pal[a], Surajit Ghosh[a], Amish G Joshi[b], Shiv Kumar[c], Swapnil Patil[a], Prince K Gupta[a], Prajyoti Singh[a], V K Gangwar[a], P Prakash[d], Ranjan K Singh[e], Eike F Schwier[c], M Sawada[c], K Shimada[c], A K Ghosh[e], Amitabh Das[d,f] and Sandip Chatterjee[a]

[a]*Department of Physics, Indian Institute of Technology (BHU) Varanasi 221005*
[b]*CSIR-National Physical Laboratory, Dr. K. S. Krishnan Road, New Delhi 110012, India*
[c]*Hiroshima Synchrotron Radiation Center, Hiroshima University, Higashi-Hiroshima City, 739-0046 Japan*
[d]*Solid State Physics Division, Bhaba Atomic Research Centre, Mumbai 400085, India*
[e]*Department of Physics, Banaras Hindu University, Varanasi 221005, India*
[f]*Homi Bhabha National Institute, Anushaktinagar, Mumbai 400094, India*

Electronic structure of Pr_2CoFeO_6 (at 300 K) was investigated by x-ray photoemission spectroscopy (XPS) and x-ray absorption spectroscopy techniques. All three cations, i.e. Pr, Co and Fe were found to be trivalent in nature. XPS valance band analysis suggested the system to be insulating in nature. The analysis suggested that Co^{3+} ions exist in low spin state in the system. Moreover, Raman spectroscopy study indicated the random distribution of the B-site ions (Co/Fe) triggered by same charge states. In temperature-dependent Raman study, the relative heights of the two observed phonon modes exhibited anomalous behaviour near magnetic transition temperature TN ~ 270 K, thus indicating towards interplay between spin and phonon degrees of freedom in the system. Furthermore, clear anomalous softening was observed below TN which confirmed the existence of strong spin–phonon coupling occurring for at least two phonon modes of the system. The line width analysis of the phonon modes essentially ruled out the role of magnetostriction effect in the observed phonon anomaly. The investigation of the lattice parameter variation across TN (obtained from the temperature dependent neutron diffraction measurements) further confirmed the existence of the spin–phonon coupling.

REFERENCES

1. S. W. Cheong and M. Mostovoy, *Nat. Mater.* **6**, 13 (2007).
2. Y. Kitagawa *et al. Nat. Mater.* **9**, 797 (2010).
3. K. I. Kobayashi, T. Kimura, H. Sawada, K. Terakura and Y. Tokura, *Nature* **395**, 677 (1998).
4. D. Choudhury *et al. Phys. Rev. Lett.* **108**, 127201 (2012).